

Modelling brain connectomes networks: Solv is a worthy competitor to hyperbolic geometry!

Dorota Celińska-Kopczyńska, Eryk Kopczyński
Institute of Informatics, University of Warsaw, Warsaw, Poland

July 24, 2024

Abstract

Finding suitable embeddings for connectomes (spatially embedded complex networks that map neural connections in the brain) is crucial for analyzing and understanding cognitive processes. Recent studies have found two-dimensional hyperbolic embeddings superior to Euclidean embeddings in modeling connectomes across species, especially human connectomes. However, those studies had limitations: geometries other than Euclidean, hyperbolic, or spherical were not considered. Following William Thurston's suggestion that the networks of neurons in the brain could be successfully represented in Solv geometry, we study the goodness-of-fit of the embeddings for 21 connectome networks (8 species). To this end, we suggest an embedding algorithm based on Simulating Annealing that allows us to embed connectomes to Euclidean, Spherical, Hyperbolic, Solv, Nil, and product geometries. Our algorithm tends to find better embeddings than the state-of-the-art, even in the hyperbolic case. Our findings suggest that while three-dimensional hyperbolic embeddings yield the best results in many cases, Solv embeddings perform reasonably well.

1 Introduction

Connectomes are comprehensive maps of the neural connections in the brain. Understanding the interactions they shape is a key to understanding cognitive processes. Given their spatially embedded complexity, shaped by physical

constraints and communication imperatives, connectomes exhibit properties inherent to non-Euclidean geometries. Therefore, a vast amount of recent research has been devoted to finding the appropriate embeddings for connectome networks. Recent studies (e.g., [WHKL22, AS20]) have advocated for the superiority of two-dimensional hyperbolic embeddings over Euclidean embeddings in modeling connectomes across species, especially human connectomes. However, those studies had limitations: they restricted the focus to Euclidean, hyperbolic, or spherical geometries, neglecting to explore other potential embedding spaces.

Our study expands the perspectives for suitable embeddings. We analyze the goodness of fit (measured with widely used quality measures) of the embeddings for 21 connectome networks (8 species) to 15 unique tessellations (Euclidean, Spherical, Hyperbolic, Solv, Nil, and also product geometries). We consider both two-dimensional and three-dimensional manifolds. Following William Thurston’s suggestion that the networks of neurons in the brain could be successfully represented in Solv geometry (one of eight so-called Thurston geometries), we stipulate that this geometry would outperform hyperbolic geometry.

Against this background, our contribution in this paper can be summarized as follows:

- We present a novel embedding method based on Simulated Annealing (SA). Experiments show that our algorithm outperforms the state-of-the-art, even for the hyperbolic embeddings, as evaluated by standard measures (mAP, MeanRank, greedy routing success, and stretch).
- To the best of our knowledge, we are the first to compare embeddings of connectomes to all Thurston geometries. As a result, we expand the horizons of connectome modeling and open up new possibilities for analysis. We show that connectome modeling is more nuanced than previously presented.
- We find that while three-dimensional hyperbolic geometry yields the best results in many cases, other geometries, such as Solv, are worth considering. Supported by an extensive simulation scheme, our results bring confidence and reliability beyond previous studies.

This paper is accompanied with supplementary material containing our implementation, data and results [CKK24a] and a video containing our 3D visualizations [CKK24b].

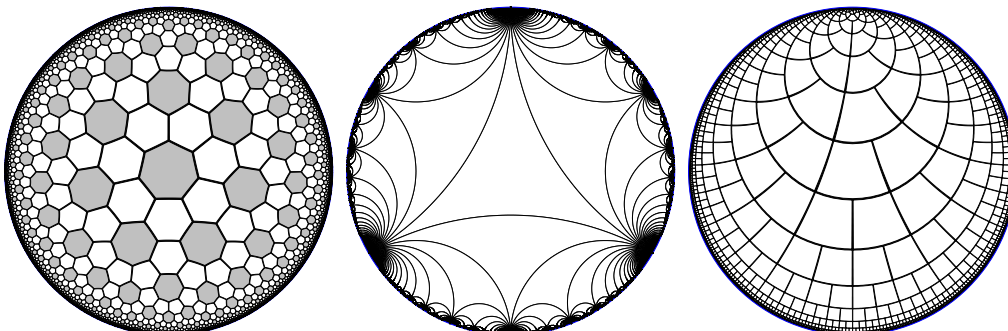


Figure 1: Tessellations of the hyperbolic plane. From left to right: (a) bitruncated order-3 heptagonal tiling ($\{7, 3\}$), (b) infinite-order triangular tiling ($\{3, \infty\}$), (c) binary tiling.

2 Prerequisites

2.1 Thurston geometries

By the uniformization theorem, every closed two-dimensional topological surface can be given spherical (\mathbb{S}^2), Euclidean (\mathbb{E}^2), or hyperbolic (\mathbb{H}^2) geometry, that is, there exists a Riemannian manifold with the same topology as M and locally isometric to a sphere, Euclidean plane, or hyperbolic plane. William Thurston conjectured [Thu82] that three-dimensional topological manifolds can be similarly decomposed into fragments, each of which can be given one of eight *Thurston geometries*, which are homogeneous Riemannian manifolds. The eight Thurston geometries include:

- isotropic geometries: spherical (\mathbb{S}^3), Euclidean (\mathbb{E}^3), and hyperbolic (\mathbb{H}^3).
- product geometries: $\mathbb{S}^2 \times \mathbb{R}$ and $\mathbb{H}^2 \times \mathbb{R}$, In geometry $\mathbb{A} \times \mathbb{B}$, the distance $d_{\mathbb{A} \times \mathbb{B}}$ between $(a_1, b_1), (a_2, b_2) \in \mathbb{A} \times \mathbb{B}$ is defined using the Pythagorean formula:

$$d_{\mathbb{A} \times \mathbb{B}}((a_1, b_1), (a_2, b_2)) = \sqrt{d_{\mathbb{A}}(a_1, a_2)^2 + d_{\mathbb{B}}(b_1, b_2)^2}.$$

Intuitively, using the Pythagorean formula here means that the third dimension is added to \mathbb{S}^2 or \mathbb{H}^2 in the Euclidean way.

- Twisted product geometries: twisted $\mathbb{E}^2 \times \mathbb{R}$, also known as Nil, and twisted $\mathbb{H}^2 \times \mathbb{R}$, referred to as Twist in this paper, also known as the universal cover of $SL(2, \mathbb{R})$. [KCK20]
- Solv geometry, also known as Solve or Sol, which is fully anisotropic.

The more exotic Thurston geometries have been successfully visualized only very recently [KCK20, CMST20], and thus are much less known than isotropic geometries. We refer to these papers and explanatory videos [Rog23, Rog22] and demos [CMST22] for detailed explanations of Solv and Nil geometries. In the rest of this section, we include a brief description of Solv and an intuitive explanation of twisted product geometries.

The n -dimensional sphere is $\mathbb{S}^n = \{x \in \mathbb{R}^{n+1} : g(x, x) = 1\}$, where g is the Euclidean inner product, $g(x, y) = x_1y_1 + x_2y_2 + \dots + x_{n+1}y_{n+1}$. The distance between two points a, b on the sphere is the length of the arc connecting a and b , which can be computed as $d(a, b) = \arccos g(a, b)$. Similarly, we can define n dimensional hyperbolic geometry using the Minkowski hyperboloid model. In this model, $\mathbb{H}^n = \{x \in \mathbb{R}^{d+1} : x_{d+1} > 0, g^-(x, x) = -1\}$, where g^- is the Minkowski inner product, $g^-(x, y) = x_1y_1 + x_2y_2 + \dots + x_ny_n - x_{n+1}y_{n+1}$. The distance between two points can be computed as $d(a, b) = \operatorname{acosh} g^-(a, b)$.

Typically, tessellations of the hyperbolic plane \mathbb{H}^2 are visualized using the Poincaré disk model, which is a projection of \mathbb{H}^2 to the Euclidean plane that distorts the distances (Figure 1). In each of these tessellations, all the shapes (of the same color) have the same hyperbolic size, even though ones closer to the boundary look smaller in the projection.

To explain Solv, we should start with the horocyclic coordinate system of \mathbb{H}^2 . Horocycles are represented in the Poincaré disk model as circles tangent to the boundary; these can be seen as hyperbolic analogs of circles with infinite radius and circumference, centered in an ideal point (point on the boundary of the Poincaré disk). Figure 1c depicts concentric horocycles; the distance between two adjacent horocycles in this picture is $\log(2)$, and if two points A and B on given horocycle are in the distance x , then the distance between their projections on the next (outer) horocycle is $2x$. For a point $P \in \mathbb{H}^2$, we project P orthogonally to Q on the horocycle going through the center C of the Poincaré model. The x coordinate is the (signed) length of the horocyclic arc CQ , and y is the (signed) length of the segment PQ . (This is similar to the upper half-plane model [CFK⁺97], except that we take the logarithm of the y coordinate.) In this coordinate system, the length of the

curve $((x(t), y(t)) : t \in [a, b])$ is defined as $\int_a^b \sqrt{(x'(t) \exp yt)^2 + y'(t)^2} dt$.

A similar coordinate system for \mathbb{H}^3 defines the length of the curve $((x(t), y(t), z(t)) : t \in [a, b])$ as $\int_a^b \sqrt{(x'(t) \exp z(t))^2 + (y'(t) \exp z(t))^2 + z'(t)^2} dt$. The surfaces of constant z are called *horospheres*; the geometry on a horosphere is Euclidean. We obtain Solv geometry by switching the sign in this formula. That is, each point also has three coordinates $(x, y, \text{ and } z)$, but the length of a curve is now equal to $\int_a^b \sqrt{(x'(t) \exp z(t))^2 + (y'(t) \exp -z(t))^2 + z'(t)^2} dt$. The distance between two points is the length of the shortest curve connecting them; this length is difficult to compute [CMST20, KCK22].

In Nil, we have well-defined directions at every point, which we can intuitively call North, East, South, West, Up and Down. However, while in Euclidean geometry, after moving 1 unit to the North, East, South, and West, we return to the starting point; in Nil, such a loop results in a move by 1 unit in the Up direction. In general, the vertical movement is equal to the signed area of the projection of the loop on the horizontal plane. Twist is based on the same idea, but the horizontal plane is now hyperbolic.

2.2 Geometric embeddings

In low-dimensional topology, three-dimensional geometry is incredibly challenging; mainly, the Poincaré conjecture was the most challenging in three dimensions. On the other hand, our interest in two-dimensional and three-dimensional geometries is based on their visualization possibilities [KCK20, CMST20] and potential application to geometric embeddings.

Figure 1 shows that hyperbolic geometry has a tree-like, hierarchical structure. This tree-likeness has found application in the visualization and modeling of hierarchical structures [LRP95, Mun98], and then in the modeling of complex networks. The hyperbolic random graph model (HRG) [BPK10] is parameterized by parameters N, R, T, α . Each node $i \in \{1, \dots, n\}$ is assigned a point $m(i)$ in the hyperbolic disk of radius R ; the parameter α controls the distribution. Then, every pair of points $a, b \in \{1, \dots, n\}$ is connected with probability $1/(1 + \exp((d - R)/T))$, where d is the hyperbolic distance between a and b . A real-world network (V, E) can be also embedded into the hyperbolic plane \mathbb{H}^2 by mapping its nodes V to \mathbb{H}^2 [BPK10]; an embedding is better if the probability of forming the actual observed connections (according to the HRG model) is higher. Moreover, graphs generated according to this model have properties typical to scale-free networks, such

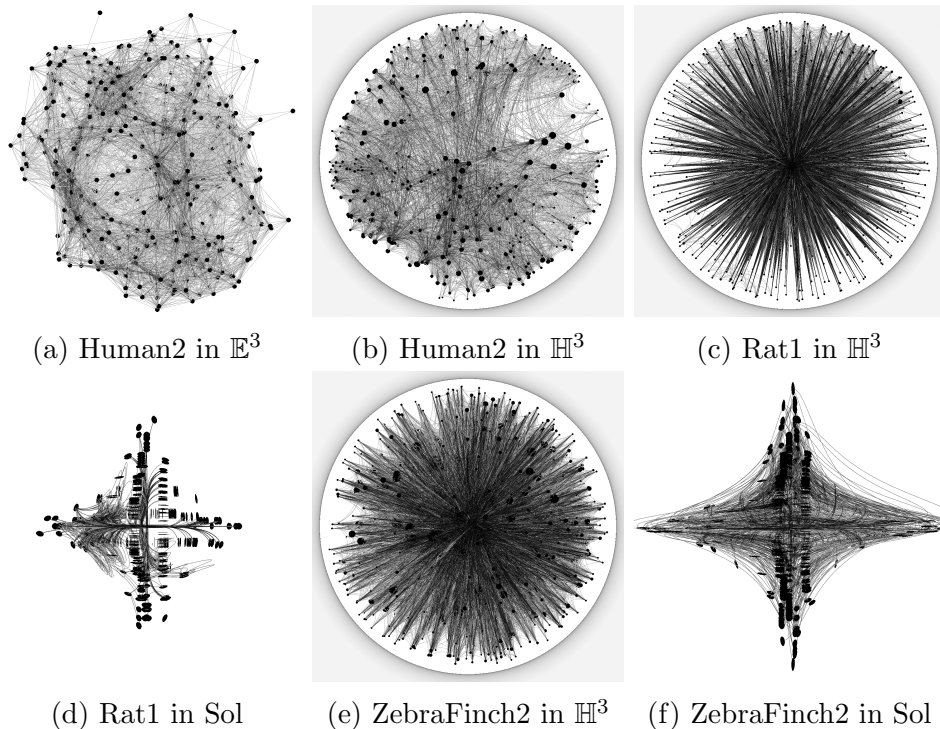


Figure 2: A 2D projection of our embeddings. See [CKK24b] for 3D visualizations.

as high clustering coefficient and power-law degree distribution [PKS⁺12].

More recently, embeddings into higher-dimensional hyperbolic spaces were studied in the network [JABS23, WHKL22] and the machine learning community (product geometries in [GSGR19]). To our knowledge, twisted product or Solv geometry have yet to be studied in this context. We are especially interested in the intriguing suggestion of William Thurston from 1997 that the brain’s architecture might be based on Solv geometry [Sch20]. Intuitively, the Solv geometry is based on two hierarchies (the hyperbolic plane $y = \text{const}$ and the hyperbolic plane $x = \text{const}$), which are opposed to each other due to the opposite sign used with z in the distance formula. This gives us hope that we can use Solv geometry to represent in three dimensions hierarchies that cannot be represented using other two- or three-dimensional geometries exhibiting simpler hierarchical structure (\mathbb{H}^2 , \mathbb{H}^3 , $\mathbb{H}^2 \times \mathbb{R}$). A similar effect of two opposing hierarchies could also be obtained in $\mathbb{H}^2 \times \mathbb{H}^2$. However, that is a four-dimensional geometry and, thus, less suitable for visualization. An

promising property of Nil geometry is that it is a three-dimensional geometry where the volume of a ball of radius R has $\Theta(R^4)$ growth, which suggests better embedding possibilities than \mathbb{E}^3 , but worse than the exponentially-expanding geometries.

3 Our contribution

We need a new embedding algorithm since the previous algorithms may be particularly tailored to the specific geometry [BFKL16], or assume that $d_{\mathbb{G}}$ is easy to compute, which is not true for Solv. We aim to find good quality embeddings of a connectome (V, E) into some geometry \mathbb{G} , that is, a map $m : V \rightarrow \mathbb{G}$. As in the hyperbolic random graph (HRG) model, we assume that our embedding has two parameters: R and T . The probability that an edge exists between i and j is $p_1(d) = 1/(1 + \exp((d - R)/T))$, where d is the distance between $m(i)$ and $m(j)$. We use MLE method to find the embedding, that is, we aim to maximize the likelihood $\prod_{1 \leq i < j \leq N} p(i, j)$, where $p(i, j) = p_1(d_{\mathbb{G}}(m(i), m(j)))$ in case if the edge between i and j exists, and $p(i, j) = 1 - p_1(d_{\mathbb{G}}(m(i), m(j)))$ otherwise. Equivalently, we maximalize the loglikelihood $\sum_{1 \leq i < j \leq N} \log p(i, j)$.

3.1 Our embedding algorithm

As in [CKK21], our algorithm is based on a uniform grid in geometry \mathbb{G} . Natural grids exist in all Thurston geometries of interest [KCK20]. In the HRG model, the network is mapped to a disk of radius R ; here, we map the network to the set D of all grid points in \mathbb{G} , which are in the distance at most d_R from some fixed origin. We choose d_R to fix the number of points inside D ; in most experiments, we pick $M = 20000$ points (actually, there may be slightly more points due to ties).

We compute the distance $d_{\mathbb{G}}$ for every pair of points in D , thus obtaining a $|D| \times |D|$ array that can be used to quickly find the distance between pairs of points. In the case of Solv, it turns out that the method to compute the Solv distances from [KCK20], while applicable to visualization, does not apply to computing this table of distances due to long ranges. Therefore, for longer distances, we approximate by $d(a, b)$ as the smallest possible $d(a, a_1) + d(a_1, a_2) + \dots + d(a_k, b)$, where intermediate points are also in D , and each pair of consecutive points is within the range of the method from [KCK20].

Dijkstra’s algorithm is used to find the path (a_i) .

Now, we use the Simulated Annealing method to find the embedding. This method assumes R and T and starts with an arbitrary embedding $m : V \rightarrow D$. Then, we perform the following for $i = 1, \dots, N_S$:

- Introduce a small change m' to the current embedding m ,
- Compute L , the loglikelihood of m , and L' , the loglikelihood of m' .
- If $L' > L$, always replace m with m' . Otherwise, replace m with m' with probability $\exp((L' - L)/\exp(T))$, where the parameter T (known as *temperature*) depends on the iteration index.

In Simulated Annealing, we start with a very high temperature (to accept all changes and thus explore the full space of possible embeddings without getting stuck on local maxima). Then we proceed to lower and lower temperatures (not accepting changes that yield much worse embeddings but still experimenting with crossing lower valleys), eventually accepting only the changes that improve the embedding. In our experiments, T decreases linearly from 10 to -15. We consider local changes of two possible forms: move $m'(i)$ for a random i to a random point in D , and move $m'(i)$ for a random i to a random point in D that is close (neighbor) to $m(i)$. These changes allow computing L' (based on the earlier L) in time $O(|V|)$.

To obtain values of R and T , we start with some initial values of R and T . Occasionally, during the simulated annealing procedure, we find the values of R and T that best fit the current embedding, and we use the new values for the remaining iterations. Since finding the correct values takes time, we do it relatively rarely (every $|V|$ iterations with successful moves) and only once the simulated annealing procedure rejects most changes. In our experiments, we repeat this setup 30 times; in the following iterations, we start with the values of R and T that were obtained in the best embedding found so far. The time complexity of an iteration is $O(N_S \cdot |V|)$.

Our implementation uses the tessellations implemented in RogueViz [KCK23] and is based on the existing implementation of Simulated Annealing for finding hyperbolic visualizations [CK17].

3.2 Visualization

In Figure 2, we present selected embeddings for the human cortex, rat nervous system, and zebra finch basal-ganglia connectomes. The embeddings

exhibit different shapes: e.g., rat nervous system connectomes are star-like, with a group of neurons in the center of the embedding connected to other neurons, with few other connections. Different geometries highlight these differences. E.g., such star-like networks embed well into \mathbb{H}^3 or trees. Our visualization engine lets the viewer rotate the embedding and examine the spatial relationships in detail. See the videos in the supplementary material.

4 Experiments

For our experiments, we use the same set of publicly available connectomes as [AS20]¹ (not all connectomes used there are publicly available). See Table 1.

We run 30 iterations of SA to find the best R and T , with $N_S = 10000 \cdot |V|$. We evaluate the quality of embeddings using the following five measures (all ranging from 0 – worst to 1 – perfect).

SC Greedy routing success rate. SC is the probability that, for random pair of vertices $(x, y) \in V^2$, the greedy routing algorithm starting at x eventually successfully reaches the target y . This routing algorithm moves in the first step from x to x_1 , the neighbor of x the closest to y (that is, $d_G(m(x_1), m(y))$ is the smallest). If $x_1 \neq y$, we continue to x_2 , the neighbor of x_1 the closest to y , and so on.

IST Greedy routing stretch. Stretch is the expected ratio of the route length found in the greedy routing procedure to the shortest route length, conditional that greedy routing was successful. IST is the reciprocal of stretch.

IMR For an edge $(x, y) \in E$, $\text{rank}(x, y)$ is one plus the number of vertices that are closer to x than y but not connected with an edge. MeanRank is the expected value of (x, y) over all edges. We use $\text{IMR} = 1/\text{MeanRank}$.

MAP For an edge $(x, y) \in E$, $P(x, y)$ is the ratio of vertices in distance of at most $d_G(m(x), m(y))$ to x which are connected with x . $AP(x)$ is the average of $P(x, y)$ for all y connected with x , and MAP is the average of $AP(X)$ over all X .

¹URL: https://github.com/networkgeometry/navigable_brain_maps_data/

name	node	zone	$ V $	$ E $	source
CElegans	cell	nervous system	279	2290	[VCP ⁺ 11]
Cat1	area	cortex	65	730	[SBY95]
Cat2	area	cortex and thalamus	95	1170	[SBH ⁺ 99]
Cat3	area	cortex	52	515	[SBH ⁺ 99]
Drosophila1	cell	optic medulla	350	2886	[SNM ⁺ 22]
Drosophila2	cell	optic medulla	1770	8904	[SNM ⁺ 22]
Macaque1	area	cortex	94	1515	[KH06]
Macaque2	area	cortex	71	438	[You93]
Macaque3	area	cortex	242	3054	[HvdHS12]
Macaque4	area	cortex	29	322	[MERL ⁺ 13]
Mouse2	cell	retina	916	77584	[HBT ⁺ 13]
Mouse3	cell	retina	1076	90810	[HBT ⁺ 13]
Human1	area	cortex	493	7773	[HCG ⁺ 08]
Human2	area	cortex	496	8037	[HCG ⁺ 08]
Human6	area	whole brain	116	1164	[GRKM ⁺ 13]
Human7	area	whole brain	110	965	[GRKM ⁺ 13]
Human8	area	whole brain	246	11060	[GRKM ⁺ 13]
Rat1	area	nervous system	503	23029	[BS07]
Rat2	area	nervous system	502	24655	[BS07]
Rat3	area	nervous system	493	25978	[BS07]
ZebraFinch2	cell	basal-ganglia (Area X)	610	15342	[DSK ⁺ 17]

Table 1: Connectomes in our experiments. From [AS20] (some labels and sizes fixed to match actual data).

NLL Last but not least, log-likelihood (LL), which is directly maximized in our algorithm, as well as in many other embedding algorithms [BFKL16, GPASB19]. For a given connectome (V, E) , the best theoretically possible log-likelihood is obtained when an edge between x and y occurs if and only if the distance $d_G(m(x), m(y))$ is below some threshold value, and thus, edges can be predicted with full certainty based on the distance (log-likelihood = 0) and the worst possible is obtained when the distance gives no information on edges, and thus, the probability of each edge is predicted as $|E|/\binom{|V|}{2}$ (log-likelihood = H). Normalized log-likelihood, NLL, is defined as $1-LL/H$.

Greedy routing measures are standards in the network science community

(e.g., [BPK10]) and MeanRank/mAP measures in the machine learning community (e.g., [NK17]). The computations of SC, STR, MR, and MAP care on the order of nodes $y \in V$ by distance from $x \in V$. However, since we are using a discrete set D , it is possible that $d_{\mathbb{G}}(m(x), m(y)) = d_{\mathbb{G}}(m(x), m(z))$ for $y \neq z$. Thus, we assume that the tied nodes are ordered randomly in the case of a tie.

We work with the 15 tessellations listed in Table 2. Most of our tessellations are hyperbolic. Subdivided(d) means that each cube of the honeycomb has been subdivided into $d \times d \times d$ subcubes, and the point D consists of the vertices and centers of these subcubes, approximating the set of centers of cells of the Euclidean bitruncated cubic honeycomb. In the case of Nil and Solv, we do not get actual cubes, so this construction is approximate.

name	dim	geometry	closed	nodes	diameter	description of the set D
\mathbb{H}^2	2	hyperbolic	F	20007	304	bitruncated $\{7, 3\}$ (Figure 1a)
$\mathbb{H}^2&$	2	hyperbolic	T	17980	157	closed hyperbolic manifold
tree	2	tree	F	20002	396	$\{3, \infty\}$ (Figure 1b)
\mathbb{E}^3	3	euclid	F	20107	1070	bitruncated cubic honeycomb
$\mathbb{E}^3&$	3	euclid	T	19683	450	torus subdivided into $27 \times 27 \times 27$ cells
\mathbb{H}^3	3	hyperbolic	F	21365	201	$\{4, 3, 5\}$ hyperbolic honeycomb
\mathbb{H}^3*	3	hyperbolic	F	20039	146	$\{4, 3, 5\}$ subdivided(2)
$\mathbb{H}^3&$	3	hyperbolic	T	9620	102	subdivided(2) closed hyperbolic manifold
Nil	3	nil	F	20009	1000	integer coordinates
Nil*	3	nil	F	20208	290	integer coordinates, subdivided(2)
Twist	3	twist	F	20138	152	twisted $\{5, 4\} \times \mathbb{Z}$
$\mathbb{H}^2 \times \mathbb{R}$	3	product	F	20049	29	bitruncated $\{7, 3\} \times \mathbb{Z}$
Solv	3	solv	F	20017	246	analog of Figure 1c
Solv*	3	solv	F	20000	143	analog of Figure 1c, subdivided(2)
\mathbb{S}^3	3	sphere	T	21384	628	8-cell, each cell subdivided(11)

Table 2: Details on tessellations used in our study; * denotes finer grids.

5 Comparison at maximum performances

We start with a naive comparison among the tessellations based on the best results obtained for each tessellation for each connectome. Figures 3, 4, 7, 6, and 5 visualize the rankings of the tessellations. 1s (the top) are the highest results, and 0s (the bottom) are the lowest for a given connectome.

According to Figures 3-5 and Tables 4 and 5, we notice that the assessment of the performance of the geometry may vary concerning the quality

connectome	NLL	MAP	IMR	SC	IST
Cat1	5.47	1.29	10.28	0.40	0.65
Cat2	4.84	3.75	8.94	1.94	1.63
Cat3	6.22	1.35	11.04	0.09	0.66
CElegans	7.46	6.05	8.38	8.89	6.30
Drosophila1	5.46	10.15	8.34	12.19	9.47
Drosophila2	12.52	32.87	11.48	27.32	25.87
Human1	9.13	5.95	29.08	11.94	7.06
Human2	9.19	6.20	28.38	11.62	7.00
Human6	7.69	3.52	26.79	7.29	4.53
Human7	8.13	3.45	25.58	7.23	4.34
Human8	6.38	1.72	17.92	0.23	0.74
Macaque1	3.95	3.93	10.21	2.87	2.21
Macaque2	7.22	3.02	16.74	6.11	3.30
Macaque3	4.99	7.52	9.05	6.88	5.84
Macaque4	9.44	0.27	4.51	0.00	0.00
Mouse2	9.68	7.54	10.86	3.78	4.94
Mouse3	10.85	8.84	10.98	3.58	5.14
Rat1	44.60	32.51	66.25	10.25	8.18
Rat2	44.32	31.33	68.97	10.02	8.13
Rat3	40.76	27.42	62.36	9.85	7.96
ZebraFinch2	14.83	19.70	7.06	16.29	12.50

Table 3: Coefficients of variations (CV, in %) for the maximum performance of the geometries per connectome

measure; there are also differences across species. In general, trees perform poorly in measures other than greedy success rate, and no matter the measure, they are always the best choice for Rat’s connectomes (nervous system). Results for Rat’s and Drosophila2’s connectomes are also characterized by the relatively high variation among species (Table 3). For other species, the best performances are similar with respect to a quality measure: the differences in best performance among geometries measured with MAP, greedy rate success, and stretch are slight (in most cases, values of CVs are under 10%); especially for Cat’s connectomes, they tend to be negligible (values of CVs even under 1%).

The results suggest that \mathbb{H}^2 and \mathbb{S}^3 seem to be inefficient choices: the

geometry	MIN					MED					MAX				
	NLL	MAP	IMR	SC	IST	NLL	MAP	IMR	SC	IST	NLL	MAP	IMR	SC	IST
\mathbb{H}^2	2	2	2	2	8	4	10	2	13	9	12	12	12	15	13
$\mathbb{H}^2\&$	1	1	1	1	1	3	4	3	1	2	6	7	6	8	8
tree	1	1	1	1	8	3	9	1	13	10	15	15	14	15	15
\mathbb{E}^3	2	2	2	1	3	5	3	6	5	5	14	15	15	13	15
$\mathbb{E}^3\&$	2	2	2	1	1	5	3	10	3	3	14.5	14.5	15	9	14
\mathbb{H}^3	4	4	3	8	6	12	13	6	11	12	15	15	15	15	15
\mathbb{H}^3*	9	8	5	6	7	12	13	10	12	14	15	15	15	15	15
$\mathbb{H}^3\&$	5	5	5	2	2	7	6	8	2	5	14	15	15	8	15
Nil	4	4	5	5	5	8	7	9	7	8	14	13	15	11	10
Nil*	4	4	4	4	5	7	5	11	6	6	14.5	14.5	15	10.5	14
Twist	4	4	4	5	4	13	13	10	11	13	15	14	14	14	15
$\mathbb{H}^2 \times \mathbb{R}$	8	8	7	8	8	12	11	12	10	11	15	15	15	12	15
Solv	5	4	4	4	5	11	10	8	10.5	10	15	15	15	14	15
Solv*	7	7	8	6	7	10	8	11	8	8	15	15	14	11	13
\mathbb{S}^3	1	1	1	1	1	2	1	4	4	2	9	15	15	9	9

Table 4: Descriptive statistics (minimum, median, maximum) for ranks obtained by geometries (at the maximum performance)

geometry	Top 5 ranks					Bottom 5 ranks				
	NLL	MAP	IMR	SC	IST	NLL	MAP	IMR	SC	IST
\mathbb{H}^2	19.05	23.81	14.29	80.95	33.33	57.14	42.86	71.43	0.00	19.05
$\mathbb{H}^2\&$	0.00	0.00	0.00	0.00	0.00	95.24	85.71	90.48	95.24	90.48
tree	23.81	23.81	14.29	80.95	47.62	66.67	42.86	80.95	0.00	28.57
\mathbb{E}^3	19.05	23.81	23.81	9.52	14.29	57.14	66.67	38.10	61.90	57.14
$\mathbb{E}^3\&$	19.05	28.57	47.62	0.00	4.76	52.38	57.14	33.33	90.48	85.71
\mathbb{H}^3	66.67	61.90	33.33	52.38	66.67	9.52	14.29	42.86	0.00	0.00
\mathbb{H}^3*	66.67	76.19	38.10	61.90	76.19	0.00	0.00	4.76	0.00	0.00
$\mathbb{H}^3\&$	9.52	19.05	28.57	0.00	4.76	14.29	14.29	4.76	90.48	66.67
Nil	19.05	9.52	33.33	4.76	0.00	4.76	9.52	4.76	4.76	9.52
Nil*	38.10	38.10	57.14	0.00	19.05	28.57	57.14	19.05	14.29	28.57
Twist	61.90	57.14	38.10	57.14	71.43	19.05	19.05	14.29	9.52	4.76
$\mathbb{H}^2 \times \mathbb{R}$	66.67	52.38	52.38	42.86	71.43	0.00	0.00	0.00	0.00	0.00
Solv	52.38	47.62	33.33	47.62	42.86	14.29	14.29	28.57	9.52	4.76
Solv*	38.10	28.57	61.90	9.52	23.81	0.00	0.00	0.00	0.00	0.00
\mathbb{S}^3	0.00	9.52	23.81	0.00	0.00	80.95	76.19	66.67	85.71	80.95

Table 5: Percentages how many times a given geometry occurred within top or bottom five ranks (at the maximum performance)

first one never enters the top five ranks; both often occur within the bottom

five ranks, at their best performance being even the worst choices no matter the quality measure. In contrast, \mathbb{H}^3 and $\mathbb{H}^2 \times \mathbb{R}$ perform very well – they rarely occur within the bottom five ranks. Twist and Solv or Solv* never happen to be the worst choices; they all perform relatively well. Interestingly, the usage of finer grids may not increase the chance of obtaining the best performance, no matter the quality measure: while for \mathbb{H}^3* vs. \mathbb{H}^3 and Solv* vs. Solv, we notice that it reduces the chance of occurring within the bottom five ranks, the best performances of non-fine grids still outperform them when it comes to the occurrences within the five top ranks. On the contrary, a finer grid for Nil significantly increases the percentage of occurrences among the five best ranks. When it comes to Euclidean geometry, the results are inconsistent. The best performances of \mathbb{E}^3 and $\mathbb{E}^3\&$ often occur among the bottom five ranks of the geometries. However, there are cases in which those geometries perform excellently, e.g., for Human connectomes.

5.1 Distribution-based comparison

Comparison of the maximum performance from the previous section gives us intuition about the optimistic scenarios and the limits for our embeddings. However, due to the nature of Simulated Annealing, the maximum values we obtained are still realizations of random variables; that is why a closer inspection, including information about the distributions of the simulation results, is needed. To this end, we will compare geometries using voting rules. In particular, we will be interested in finding Condorcet winners and losers. As Condorcet winner may not exist in the presence of ties, we will refer to its simple modification: Copeland rule [MD04].

Geometry A wins against geometry B if the probability that (for a given quality measure) a randomly chosen simulation result obtained by A is greater than a randomly chosen simulation result obtained by B exceeds 0.5. If that probability is equal to 0.5, we have a tie between A and B; otherwise, A loses against B. To compute the score for a given geometry, we add 1 for every winning scenario, 0 for every tie, and -1 for every losing scenario. The geometries with the highest and lowest scores become Copeland winners and losers, respectively (we allow for multiple candidates in both cases).

The winners based on the Copeland method beat most of the other candidates in pairwise contests. They should be the best options for embeddings. Based on the data in Table 6, we cannot name one universal winner. While it seems that \mathbb{H}^3 is a sound choice, we also notice that Solv and Twist are

connectome	Copeland winners					Copeland losers				
	NLL	MAP	IMR	SC	IST	NLL	MAP	IMR	SC	IST
Cat1	Solv*	\mathbb{H}^3_*	Solv*	\mathbb{H}^3_*	Solv*	$\mathbb{H}^2\&$	tree	tree	$\mathbb{H}^2\&$	tree
Cat2	\mathbb{H}^3_*	\mathbb{H}^3_*	$\mathbb{H}^2 \times \mathbb{R}$	Twist	$\mathbb{H}^2 \times \mathbb{R}$	$\mathbb{H}^2\&$	\mathbb{S}^3	tree	$\mathbb{H}^3\&$	tree
Cat3	Solv*	Solv*	$\mathbb{H}^3\&$	Nil*	$\mathbb{H}^3\&$	$\mathbb{H}^2\&$	tree	tree	$\mathbb{H}^2\&$	tree
CElegans	\mathbb{H}^3_*	\mathbb{H}^3	Nil	\mathbb{H}^3_*	Nil	$\mathbb{H}^2\&$	$\mathbb{H}^2\&$	tree	$\mathbb{H}^2\&$	tree
Drosophila1	Twist	\mathbb{H}^3	$\mathbb{H}^3\&$	\mathbb{H}^3	$\mathbb{H}^3\&$	$\mathbb{H}^2\&$	\mathbb{S}^3	tree	$\mathbb{H}^2\&$	tree
Drosophila2	\mathbb{H}^3	\mathbb{H}^3	\mathbb{H}^3_*	\mathbb{H}^3	\mathbb{H}^3_*	\mathbb{S}^3	\mathbb{S}^3	\mathbb{S}^3	$\mathbb{H}^3\&$	\mathbb{S}^3
Human1	\mathbb{E}^3	\mathbb{S}^3	\mathbb{S}^3	\mathbb{H}^3_*	\mathbb{S}^3	tree	tree	tree	$\mathbb{H}^2\&$	tree
Human2	\mathbb{E}^3	\mathbb{S}^3	\mathbb{S}^3	\mathbb{H}^3_*	\mathbb{S}^3	tree	tree	tree	$\mathbb{H}^2\&$	tree
Human6	\mathbb{E}^3	\mathbb{E}^3	\mathbb{E}^3	\mathbb{H}^3_*	\mathbb{E}^3	tree	tree	tree	$\mathbb{H}^2\&$	tree
Human7	\mathbb{E}^3	\mathbb{E}^3	\mathbb{E}^3	Solv	\mathbb{E}^3	tree	tree	tree	$\mathbb{H}^2\&$	tree
Human8	\mathbb{H}^3_*	\mathbb{H}^3_*	\mathbb{E}^3	\mathbb{H}^2	\mathbb{E}^3	tree	tree	tree	$\mathbb{H}^2\&$	tree
Macaque1	Solv	Solv	Solv	\mathbb{H}^3_*	Solv	\mathbb{S}^3	\mathbb{S}^3	tree	$\mathbb{E}^3\&$	tree
Macaque2	Nil	Nil	Nil*	\mathbb{H}^2	Nil*	tree	tree	tree	$\mathbb{H}^2\&$	tree
Macaque3	\mathbb{H}^3_*	\mathbb{H}^3_*	$\mathbb{H}^2 \times \mathbb{R}$	\mathbb{H}^2	$\mathbb{H}^2 \times \mathbb{R}$	$\mathbb{H}^2\&$	\mathbb{S}^3	tree	$\mathbb{H}^2\&$	tree
Macaque4	$\mathbb{E}^3\&$	$\mathbb{E}^3\&$	$\mathbb{E}^3\&$	Twist	$\mathbb{E}^3\&$	tree	tree	tree	\mathbb{E}^3	tree
Mouse2	Twist	\mathbb{H}^3	$\mathbb{H}^2 \times \mathbb{R}$	\mathbb{H}^2	$\mathbb{H}^2 \times \mathbb{R}$	\mathbb{S}^3	\mathbb{S}^3	$\mathbb{H}^2\&$	\mathbb{S}^3	$\mathbb{H}^2\&$
Mouse3	Twist	\mathbb{H}^3	$\mathbb{H}^2 \times \mathbb{R}$	\mathbb{H}^2	$\mathbb{H}^2 \times \mathbb{R}$	\mathbb{S}^3	\mathbb{S}^3	\mathbb{S}^3	$\mathbb{H}^2\&$	\mathbb{S}^3
Rat1	tree	tree	\mathbb{H}^3	tree	\mathbb{H}^3	\mathbb{S}^3	\mathbb{S}^3	\mathbb{S}^3	\mathbb{S}^3	\mathbb{S}^3
Rat2	tree	tree	\mathbb{H}^3	tree	\mathbb{H}^3	\mathbb{S}^3	\mathbb{S}^3	\mathbb{S}^3	$\mathbb{E}^3\&$	\mathbb{S}^3
Rat3	tree	tree	\mathbb{H}^3	tree	\mathbb{H}^3	\mathbb{S}^3	\mathbb{S}^3	\mathbb{S}^3	\mathbb{S}^3	\mathbb{S}^3
ZebraFinch2	Solv	\mathbb{H}^3	Solv	\mathbb{H}^3	Solv	\mathbb{S}^3	\mathbb{S}^3	\mathbb{S}^3	Solv	\mathbb{S}^3

Table 6: Voting rules: Copeland winners and losers.

worthy of attention. Interestingly, for Human connectomes, \mathbb{E}^3 outperforms other geometries.

In Figures 8-12, we provide weighted directed networks constructed upon the voting rules to allow for generalizations. The weights correspond to the percent of connectomes for which the source geometry in the edge beats the target geometry. Embeddings to Twist have a 100% success rate over embeddings in \mathbb{H}^2 (for quality measures different than greedy routing success).

5.2 Zone-function-based comparison

We have already shown that, contrary to previous results from the literature, we cannot name one universal best geometry to model any connectome. A new interesting question arises if there are relationships between the function of the connectome (based on its zone) and the suitability of the geometries (using the rankings from the distribution-based comparisons). To find out, we analyze the values of intraclass correlation coefficients (ICC), a widespread tool in the assessment of consistency among multiple raters [SF79] when the rating scale is ordinal to continuous. The literature suggests that the values of ICC below 0.50 indicate poor agreement, between 0.50 and 0.90 suggest moderate to good agreement, and above 0.90: an excellent one [KL16]. To obtain an aggregate ranking for the whole zone, for each measure and each geometry we computed the median of its minus rank (the minus gives us information 50% of ranks achieved by the given geometry are at least this high in modelling given zone, the lower values, the better). Medians were chosen due to their immunity to outliers.

According to data in Table 7, the intra-zone comparisons suggest good to excellent agreement no matter the quality measure. Rankings for connectomes from “other” zone (usually specific cells, e.g., from retina or optic medulla) show relatively lower agreement. On the contrary, the inter-zone comparison suggests poor to moderate agreement between the rankings. While the p-values in significance tests for ICCs in inter-zone comparisons suggest significance at any reasonable significance level (even after Bonferroni corrections), the results for intra-zone comparison after Bonferroni corrections appear insignificant (so any similarities might be random), apart from the result for the SC measure. Those results are promising for us. They suggest that the choice of the suitable geometry may depend on the function of the connectome. For example, our results suggest that the trees are best choice in modelling nervous systems (no matter the quality measure), for cortex \mathbb{H}^3* , $\mathbb{H}^2 \times \mathbb{R}$, Nil^* or Solv^* would be a suitable choice, and Twist may be beneficial for modelling specific cells.

While a natural question arises about the anatomical implications of different best fits for geometries, as well as why different connectomes might have different best geometries, answering this question in a statistically robust manner would require a more detailed study on a bigger number of sample connectomes.

measure	cortex	nervous	other	inter-zone
NLL	0.918 (0.836;0.968) p = 7.61e-16	0.944 (0.877;0.979) p = 6.98e-13	0.834 (0.663;0.936) p = 6.31e-08	0.659 (0.164;0.878) p = 0.00964
MAP	0.8 (0.597;0.922) p = 1e-06	0.977 (0.949;0.991) p = 9.83e-20	0.8 (0.593;0.923) p = 1.59e-06	0.693 (0.25;0.89) p = 0.00505
IMR	0.918 (0.836;0.968) p = 7.61e-16	0.944 (0.877;0.979) p = 6.98e-13	0.834 (0.663;0.936) p = 6.31e-08	0.659 (0.164;0.878) p = 0.00964
IST	0.918 (0.836;0.968) p = 7.61e-16	0.944 (0.877;0.979) p = 6.98e-13	0.834 (0.663;0.936) p = 6.31e-08	0.659 (0.164;0.878) p = 0.00964
SC	0.891 (0.782;0.958) p = 1.98e-12	0.97 (0.935;0.989) p = 9.57e-18	0.943 (0.884;0.978) p = 9.06e-20	0.931 (0.834;0.975) p = 5.83e-09

Table 7: The agreements between the rankings obtained for intra-zone and inter-zone rankings of geometries (values of two-way mixed effects, absolute agreement, multiple xraters ICCs). 95% confidence intervals in brackets.

6 Robustness checks and threats to validity

Ideally, there exists optimal embedding of (V, E) into the whole geometry \mathbb{G} , where $m_{\text{opt}} : V \rightarrow \mathbb{G}$, and some values of R and T are used. Unfortunately, the embedding m found by Simulated Annealing might be worse than m_{opt} due to the following issues:

- The radius d_R is too small, making m_{opt} simply not fit,
- The grid used is too coarse, hence the necessity of making $m(i)$ the grid point to closest to $m_{\text{opt}}(i)$, and thus reducing the log-likelihood,
- The number of iterations of Simulated Annealing, N_S , is too small – while Simulated Annealing is theoretically guaranteed to find the optimal embedding for given R and T with high probability as N_S tends to infinity, in practice, we are constrained by computation time limits,

- The values of the parameters R and T have not been chosen correctly.

In this section, we will explain how we combated those issues. We will also check if they affected our results.

Possibly insufficient size of grids. For comparability, we aimed to keep the number of neurons as close to 20,000 as possible. However, one could argue if this is enough. To combat the first two issues, in some geometries, we consider coarser and finer grids: coarser grids are better at handling the first issue, and finer grids are better at handling the second issue – in both cases, we expect that increasing d_R and grid density beyond some threshold yields diminishing returns. That is why, based on the results from the previous sections, we have added the so-called *big* versions – coarser but larger grids ($M = 100000$) – for selected, promising manifolds (\mathbb{H}^3 , \mathbb{H}^3* , $\mathbb{H}^2 \times \mathbb{R}$, Solv, and Twist). We will denote them with ****. See Table 8 for the details.

name	dim	geometry	closed	nodes	diameter	description of the set D
\mathbb{H}^3 **	3	hyperbolic	F	100427	233	$\{4, 3, 5\}$ hyperbolic honeycomb
(\mathbb{H}^3*) **	3	hyperbolic	F	100641	179	$\{4, 3, 5\}$ subdivided(2)
Twist**	3	twist	F	101230	184	twisted $\{5, 4\} \times \mathbb{Z}$
$\mathbb{H}^2 \times \mathbb{R}$ **	3	product	F	100030	282	bitruncated $\{7, 3\} \times \mathbb{Z}$
Solv	3	solv	F	100041	310	as in [KCK20]

Table 8: Details on tessellations used in our study (*big* versions); * denotes finer grids.

We started by checking for significant differences in favor of *big* versions of manifolds; to this end, we performed Wilcoxon tests with Bonferroni correction for multiple comparisons. Figure 13 depicts the procedure results. According to our results, in most cases, the differences are insignificant, which suggests that the size of the manifold is not a severe threat to validity. Usage of *big* versions usually results in better embeddings for Rat connectomes, which might correlate with a different function of those connectomes compared to others in the sample (they describe nervous systems). Rarely, *big* versions yield worse embeddings than the standard ones – usually for Human connectomes; however, no pattern-enabling explanation is noticeable here.

Next, we checked if the size of the manifolds affects rankings. To this end, we computed weighted Cohen’s kappas [Coh68]. In kappas, 0 represents the amount of agreement expected from random chance, and 1 signifies a perfect

agreement between the raters. Initially, kappas take into account only the agreements of the raters. The weighted kappas allow disagreements to be weighted differently, which is more suitable for us – we are more interested in the relative placement of the pairs of the geometries in the ranking than in the actual places. If there are slight differences in ranks by two raters, e.g., by one, the ranks should remain similar to us as embeddings yielding comparable quality results should still be close to each other. Although there are no universal guidelines for interpreting of those coefficients, the literature suggests that the values over 0.61 indicate moderate to substantial agreement between raters and values exceeding 0.81 – strong to almost perfect agreement [LK77].

Pair of rankings	Max performance					Copeland				
	NLL	MAP	IMR	SC	IST	NLL	MAP	IMR	SC	IST
Standard _{S_A:10,000} vs Big _{S_A:10,000}	0.80 (0.72;0.88)	0.75 (0.66;0.84)	0.84 (0.77;0.90)	0.57 (0.40;0.73)	0.61 (0.47;0.74)	0.86 (0.79;0.93)	0.81 (0.74;0.88)	0.91 (0.87;0.95)	0.71 (0.61;0.82)	0.78 (0.69;0.88)
Standard _{S_A:100,000} vs Big _{S_A:100,000}	0.78 (0.69;0.88)	0.75 (0.65;0.85)	0.85 (0.79;0.91)	0.52 (0.34;0.70)	0.65 (0.53;0.77)	0.85 (0.77;0.92)	0.83 (0.76;0.89)	0.84 (0.77;0.91)	0.75 (0.66;0.84)	0.82 (0.73;0.90)
Standard _{S_A:10,000} vs Standard _{S_A:100,000}	0.95 (0.92;0.97)	0.93 (0.90;0.96)	0.93 (0.90;0.96)	0.86 (0.80;0.92)	0.87 (0.81;0.92)	0.84 (0.77;0.90)	0.82 (0.74;0.89)	0.83 (0.76;0.91)	0.77 (0.66;0.88)	0.83 (0.75;0.91)
Big _{S_A:10,000} vs Big _{S_A:100,000}	0.76 (0.66;0.86)	0.70 (0.59;0.82)	0.78 (0.69;0.87)	0.73 (0.59;0.86)	0.60 (0.44;0.75)	0.79 (0.70;0.88)	0.75 (0.66;0.84)	0.86 (0.80;0.91)	0.69 (0.55;0.83)	0.76 (0.66;0.87)
Standard _{S_A:10,000} vs Big _{S_A:100,000}	0.74 (0.63;0.85)	0.74 (0.64;0.83)	0.79 (0.70;0.89)	0.51 (0.35;0.68)	0.68 (0.56;0.8)	0.76 (0.67;0.85)	0.76 (0.67;0.85)	0.82 (0.75;0.90)	0.58 (0.44;0.72)	0.79 (0.69;0.89)

Table 9: The agreements between the rankings obtained for different simulation setups (values of Cohen’s kappa). Standard includes: \mathbb{H}^3 , \mathbb{H}^3* , $\mathbb{H}^2 \times \mathbb{R}$, Solv, and Twist. 95% confidence intervals in brackets.

According to data in Table 9, rankings obtained from *big* versions of manifolds in the standard setup of Simulated Annealing ($N_s = 10,000$ iterations) are at least in substantial agreement with rankings based on standard versions. The high agreement in rankings based on voting rules is unsurprising. It aligns with the results depicted in Figure 13 – we include more information from the distributions, so the results should be more robust than those based on max performance (outliers). However, we recommend cautiously treating the results for greedy routing success and stretch.

Possibly insufficient number of iterations. As Simulated Annealing is a probabilistic technique for approximating the global optimum of a given function, one could argue that, e.g., increasing the number of iterations could improve our results (the third issue). The main paper describes the results obtained with Simulated Annealing with $N_s = 10,000 \cdot |V|$ iterations per simulation iteration. We also checked if our results differ if we perform Simulated Annealing with $N_s = 100,000 \cdot |V|$ iterations per simulation iteration

instead. As expected, for log-likelihood, MAP, and MR, we cannot reject the hypotheses that the results obtained with larger numbers of iterations are usually better. However, surprisingly, for greedy success rate and stretch, the results worsen with the increase in the number of iterations (Figure 14 depicts the results of Wilcoxon tests with Bonferroni correction for multiple comparisons).

We checked if the number of iterations for Simulated Annealing N_s affected our results regarding rankings with Cohen’s kappas. Based on the data in Table 9, we notice that pairs of rankings are in at least substantial agreement. The results regarding standard grids (presented in the main part of the paper) are robust to N_s – the values of kappas for optimistic scenarios are over 0.85. For rankings based on voting rules, they usually exceed 0.80. Although the agreements of rankings, if we change N_s for *big* grids, are still satisfying (most values of kappas over 0.75), the results from comparison of rankings based on standard grids with shorter time for Simulated Annealing against the *big* grids with longer time for Simulated Annealing suggests that the *big* versions of grids might be affected by N_s . Again, we notice that greedy routing success rate and stretch are less immune to the setup of Simulating Annealing, so we suggest caution while generalizing the results obtained for them.

Alternative methods of obtaining R and T The fourth issue is challenging. As explained in Section 4, the values of R and T have been obtained by dynamically adjusting them during the simulated annealing process (A). We have also experimented with other methods: R is changed, but T remains fixed (B), and both R and T remain fixed. We run 30 iterations using method (A), then 30 iterations using method (B), then 30 iterations using method (C). The fixed values of R and T are based on the best result (by log-likelihood) obtained in the earlier iterations.

If the methods change the results, we should notice level shifts in the time series of the quality measures’ values – level shifts appear as a parallel movement of the trend line. That is why we started by identifying possible locations of the level shifts in our results. Most of the time series (determined by a pair animal and geometry) has two level shifts – around the 30th and 60th iterations that correspond to the starting points of new methods (Figure 15).

We use OLS regressions to understand the impact of the change in method

on the values of the quality measures. We control for the characteristics of connectomes: number of nodes in the connectome n , number of edges in the connectome m , its *density*, *assortativity* and *clustering* coefficients, and the *zone* of the connectome; we also take into account the number of available *cells* in the grid and its *geometry*.

	100-NLL		100-mAP		100-IMR		100-SC		100-ISTR	
	Estimate	$P(> t)$	Estimate	$P(> t)$	Estimate	$P(> t)$	Estimate	$P(> t)$	Estimate	$P(> t)$
(Intercept)	4.737e+00	0.00	2.719e+01	0.00	-4.323e+01	0.00	8.118e+01	0.00	6.930e+01	2.205e-01
n	4.876e-03	0.00	-1.050e-02	0.00	-1.561e-02	0.00	-1.857e-02	0.00	-1.799e-02	1.011e-04
m	-6.801e-05	1.65e-11	-1.553e-04	0.00	7.865e-05	1.81e-10	1.032e-04	0.00	6.741e-05	5.579e-06
density	-2.428e-01	0.00	9.127e-02	0.00	-8.497e-01	0.00	1.545e-01	0.00	8.551e-02	5.370e-03
assort	1.302e+01	0.00	3.379e+01	0.00	-1.687e+01	0.00	1.431e+01	0.00	3.645e+00	1.991e-01
cluster	8.659e+01	0.00	8.163e+01	0.00	1.428e+02	0.00	1.539e+01	0.00	2.998e+01	2.854e-01
nervous	-1.061e+00	5.37e-07	-6.122e+00	0.00	-3.455e+01	0.00	1.285e+00	0.00	-2.679e+00	1.169e-01
other	1.564e+00	0.00	-3.702e+00	0.00	-2.141e+00	0.00	-3.542e+00	0.00	-3.940e-01	9.186e-02
cells	2.347e+00	2.94e-15	4.730e+00	0.00	3.912e+01	0.00	1.425e+00	2.36e-15	4.654e-01	1.642e-01
hyperbolic	8.233e+00	0.00	9.441e+00	0.00	-3.735e-01	0.109924	8.125e+00	0.00	7.031e+00	1.057e-01
other	9.250e+00	0.00	9.527e+00	0.00	3.351e-01	0.202089	6.862e+00	0.00	6.473e+00	1.189e-01
product	8.502e+00	0.00	7.357e+00	0.00	7.195e-01	0.006128	6.931e+00	0.00	6.187e+00	1.188e-01
solv	7.399e+00	0.00	6.787e+00	0.00	8.688e-01	0.000372	5.140e+00	0.00	4.747e+00	1.104e-01
nodes	3.950e-05	0.00	4.645e-05	0.00	1.631e-05	0.00	2.202e-05	0.00	2.445e-05	6.950e-07
B	-7.985e-01	5.76e-12	-5.009e-01	4.18e-07	-2.787e-01	0.049061	-4.759e-01	1.19e-11	-5.433e-01	6.406e-02
C	5.925e-01	3.30e-07	4.841e-01	1.02e-06	6.684e-01	2.41e-06	3.999e-01	1.23e-08	3.746e-01	6.412e-02
R^2 (adjusted R^2)	0.8061 (0.806)		0.8948 (0.8948)		0.8426 (0.8245)		0.8194 (0.8193)		0.8784 (0.8784)	
p-value for F-test	0.00		0.00		0.00		0.00		0.00	

Table 10: OLS regression results for the determinants of the quality measures. Number of observations = 24,536.

For all the quality measures, we notice that, on average, method B leads to lower values of the respective quality measures, and method C increases the values of the respective quality measures in comparison to results obtained with method A, *ceteris paribus* (Table 10). The differences are statistically significant. However, even if we are aware that with the increase in the number of observations, the p-values drop to zero, we work here with the multilevel categorical variables, so we are unable to comment on the size of the effect (available methods based on partial regressions and R^2 coefficients would allocate the impact to the constant term). The regressions have substantial explanatory power (R^2 coefficients at least 80%).

To sum up, if one is interested in optimizing the quality measures, we recommend using method B. We know that our choice of method A for Simulated Annealing may affect the final results; in particular, our “best” evaluations may not be optimal. However, there are at least two advantages of our approach. First, allowing the algorithm to optimize does not favor any of the tessellations – all of them have the same chances to find an optimal solution. This way, we ensure the comparability of our results. We have observed that the first iteration may yield worse results due to the poor

initially guessed values of R and T ; however, in further experiments, while the initial values of R and T change, it only affects the results a little. Eventually, we get independently distributed data, i.e., there is no serial correlation (all p-values in the Ljung-Box test smaller than 10^{-5}), which makes statistical analysis of the results significantly easier.

Alternative methods of computing distances. By a distance between two points $a, b \in D$, we mean the length of the shortest geodesic between a and b . Another option is the graph distance, where two points in D are connected when they correspond to adjacent tessellation tiles. In the case of the product geometry $\mathbb{H}^2 \times \mathbb{R}$, we could compute the angular distance, which is, intuitively, how small an object at b appears to an observer placed at a , assuming that the light travels along geodesics. To pick the method of measuring the distances in our experiment, we started with the preliminary list of tessellations shown in Table 11.

name	dim	geometry	closed	nodes	diameter	description of the set D
\mathbb{H}^2 (d)	2	hyperbolic	F	27000	560	bitruncated $\{7, 3\}$ (Figure 1a)
\mathbb{H}^2 (c)	2	hyperbolic	F	27007	316	bitruncated $\{7, 3\}$ (Figure 1a)
tree (c)	2	tree	F	20002	396	$\{3, \infty\}$ (Figure 1b)
tree (d)	2	tree	F	24574	520	binary tree
\mathbb{H}^3 (c)	3	hyperbolic	F	40979	214	$\{4, 3, 5\}$ hyperbolic honeycomb
\mathbb{H}^3 (d)	3	hyperbolic	F	41511	280	$\{4, 3, 5\}$ hyperbolic honeycomb
$\mathbb{H}^2 \times \mathbb{R}$ (c)	3	product	F	20049	222	bitruncated $\{7, 3\}$ times \mathbb{Z}
$\mathbb{H}^2 \times \mathbb{R}$ (a)	3	product	F	20022	5637	bitruncated $\{7, 3\}$ times \mathbb{Z}

Table 11: Details on the preliminary tessellations used in our study.

In the tessellations marked with (d), distances are computed as the lengths of the shortest paths in the graph (D, E_D) where two points in D are connected when they correspond to adjacent tessellation tiles. In contrast, in the tessellations marked with (c), distances are computed according to the underlying geometry. The sets D used in each pair are roughly the same size (we have less control over $|D|$ in discrete tessellations). In the case of the product geometry $\mathbb{H}^2 \times \mathbb{R}$, we compare geometric distances (c) to angular distance (a). The angular distance $d_a(X, Y)$ is, intuitively, how small an object at Y appears to an observer placed at X , assuming that the light travels along geodesics. The angular size of an object in distance d is proportional to $1/d$ in the Euclidean case and $1/\exp(d)$ in the hyperbolic case; for anisotropic geometries, it may depend on the axis. More precisely, $d_a(X, Y)$

is proportional to $\lim_{r \rightarrow 0} r^2/p(X, Y, r)$, where $p(X, Y, r)$ is the probability that a random geodesic starting in X passes within a distance of at least r from Y . For technical reasons, distances are rounded to the nearest integer multiple of $1/20$ absolute unit (for continuous distances) and multiplied by 20 (for discrete distances), except for the sphere, where the unit is $1/200$ of absolute unit. Thus, a diameter of 316 for a continuous tessellation is 15.8 absolute units; the diameter of 560 for a discrete tessellation is 28 steps, and the sphere has a diameter (i.e., half the circumference) π .

It was not certain if we benefit from those technical subtleties. As the data is not normally distributed and the sample sizes are small (30 observations), we performed Wilcoxon tests (with Bonferroni correction for multiple comparisons). Figure 16 visualizes the results of the procedure. We notice that we generally do not benefit from discrete versions of hyperbolic tessellations, which is why we decided to exclude them from further analysis. In the case of trees, we notice that the discrete version yields significantly better results for greedy success rates, so we keep that tessellation. Finally, we excluded the angular version of product geometry $\mathbb{H}^2 \times \mathbb{R}$ – we did not notice systematic gains compared to the non-angular version.

Our results vs previous approaches We compare the performance of our embedder against the previous embedders on the CElegans, Cat2, Drosophila1, Human1, Human6, Macaque3, and Mouse3 connectomes. For \mathbb{H}^2 , we have compared against the BFKL embedder [BFKL16], Mercator [GPASB19] (fast and full version), 2D Poincaré embeddings [NK17] and 2D Lorentz embeddings [NK18]. We ran each competing algorithm five times, found the best result of these 25 runs, and compared them to our results. We have also performed a similar analysis for \mathbb{H}^{3*} against 3D Poincaré and Mercator [JABS23] embeddings. Tables 12, 13, 14 and 15 list our results for four measures (we omit log-likelihood since not all embedders are based on MLE). We use the benchmark from [Ano24].

In most cases, our result turned out to give better results on mAP measures in all 30 runs, and in nearly all cases, we have received better results in most of the runs. We have not managed to beat the state of the art for Rat and Drosophila2, probably due to the large radius required for good embeddings of these connectomes. The results are also very good on MR, although we have not managed to beat Poincaré 2D embeddings on CElegans and Lorentz 2D embeddings on Human1. Mercator embed-

dings often turn out to be better on SC and IST measures. Furthermore, our embeddings use a smaller radius (7.7 for \mathbb{H}^2 , 3.7 for \mathbb{H}^3), and use less time than Lorentz or Poincaré embeddings (about 220 seconds per run on Mouse3 in \mathbb{H}^3). A smaller radius means that our embeddings avoid numerical precision issues that tend to be a serious issue in hyperbolic embeddings [BFKK18, SDSGR18, CKK21], are better able to use both the large-scale (tree-like) and smaller-scale (Euclidean-like) nature of hyperbolic geometry (while large radius embeddings tend to be tree-like) and make them more applicable for visualization. (In large-radius visualizations, fewer nodes are visible.)

7 Conclusions

In this paper, we presented an experimental analysis of embeddings of 21 connectomes to various geometries (both three-dimensional and two-dimensional). To our knowledge, we are the first to compare embeddings of connectomes to all Thurston geometries. Our findings unveil new prospects for connectome modeling, introducing a novel method based on Simulated Annealing. Our results demonstrate the efficacy of this approach – it yields superior embeddings compared to the state-of-the-art.

Although previous studies suggested that one could find a universal winner geometry for the embeddings (usually pointing at two-dimensional hyperbolic geometry), our results reveals a nuanced scenario when considering the third dimension. We showed that the universal winner ceases to exist when we consider the third dimension. In particular, \mathbb{H}^2 embeddings tend to be worse than (non-Euclidean) 3D geometries, even if our \mathbb{H}^2 embeddings are good – better than [BFKL16, GPASB19, NK17, NK18]. If we were to suggest a set of geometries to pay attention to when modeling connectomes, we would mention three-dimensional hyperbolic geometry, Solv, and product geometries. Surprisingly, three-dimensional Euclidean geometry is a suitable choice for Human connectomes. There is a correlation between the zone of the connectome (also its primary function) and the best choice for the embedding, e.g., nervous systems tend to be well modeled by trees.

Some technicalities that do not matter (discrete versions or angularity). However, the size of the grid or the setup of the Simulated Annealing can affect the results. Remarkably, in some experiment, standard grid versions have given significantly better results than the so-called *big* versions. Since

connectome	dim	mAP	method	rad	time	ours	better
CElegans	2	0.500	Poincaré	7.2	278	0.540	30
CElegans	3	0.583	Poincaré	10.1	274	0.584	21
Cat1	2	0.888	Mercator (full)	10.0	0	0.877	10
Cat1	3	0.880	Lorentz	9.2	104	0.934	30
Cat2	2	0.804	Mercator (full)	12.2	0	0.825	29
Cat2	3	0.831	Poincaré	10.7	277	0.861	30
Cat3	2	0.911	Poincaré	9.7	291	0.916	23
Cat3	3	0.911	Lorentz	9.2	86	0.952	30
Drosophila1	2	0.435	Mercator (full)	24.6	0	0.483	30
Drosophila1	3	0.495	Lorentz	10.5	248	0.512	29
Drosophila2	2	0.475	Mercator (full)	34.4	0	0.346	0
Drosophila2	3	0.393	Poincaré	12.2	912	0.360	0
Human1	2	0.654	Lorentz	11.7	1554	0.675	29
Human1	3	0.722	Poincaré	9.4	827	0.799	30
Human2	2	0.649	Lorentz	9.8	601	0.671	29
Human2	3	0.720	Lorentz	9.3	596	0.804	30
Human6	2	0.811	Lorentz	11.0	128	0.841	30
Human6	3	0.832	Lorentz	11.5	128	0.915	30
Human7	2	0.816	Mercator (full)	8.5	0	0.826	29
Human7	3	0.836	Poincaré	9.5	484	0.913	30
Human8	2	0.845	BFKL	4.0	2	0.871	30
Human8	3	0.865	Mercator	13.1	114	0.922	30
Macaque1	2	0.914	Mercator (full)	17.8	0	0.932	26
Macaque1	3	0.883	Poincaré	12.2	150	0.957	30
Macaque2	2	0.792	Lorentz	10.5	80	0.821	20
Macaque2	3	0.810	Lorentz	10.8	80	0.865	30
Macaque3	2	0.587	Mercator (full)	22.5	0	0.614	30
Macaque3	3	0.605	Poincaré	9.8	315	0.647	30
Macaque4	2	0.984	Mercator (full)	14.0	0	0.992	29
Macaque4	3	0.991	Mercator	7.8	11	0.998	30
Mouse2	2	0.604	Mercator (full)	28.8	0	0.625	30
Mouse2	3	0.672	Lorentz	12.7	5172	0.667	1
Mouse3	2	0.585	Mercator (full)	29.9	0	0.612	30
Mouse3	3	0.655	Lorentz	12.4	6068	0.655	10
Rat1	2	0.966	Mercator (full)	26.1	0	0.766	0
Rat1	3	0.951	Lorentz	14.5	1664	0.679	0
Rat2	2	0.970	Mercator (full)	30.7	0	0.777	0
Rat2	3	0.930	Lorentz	14.5	1710	0.691	0
Rat3	2	0.969	Mercator (full)	20.8	0	0.803	0
Rat3	3	0.887	Lorentz	14.5	1836	0.724	0
ZebraFinch2	2	0.325	Mercator (full)	21.4	0	0.323	2
ZebraFinch2	3	0.317	Lorentz	6.1	1086	0.310	1

Table 12: Our embeddings vs. state-of-the-art. For each connectome and dimension, we list the best prior method and its result, the radius of the embedding, time elapsed in seconds, the best result of our method, and how many times (out of 30) our result was better. MAP measure.

connectome	dim	MeanRank	method	rad	time	ours	better
CElegans	2	31.0	Poincaré	7.2	267	30.1	1
CElegans	3	26.6	Poincaré	10.3	270	26.3	18
Cat1	2	3.8	Mercator (full)	10.0	0	3.1	30
Cat1	3	4.0	Mercator	9.7	19	2.0	30
Cat2	2	7.1	Poincaré	12.2	565	5.6	30
Cat2	3	6.2	Poincaré	10.1	570	4.3	30
Cat3	2	3.2	Mercator (full)	6.5	0	1.9	30
Cat3	3	3.1	Mercator	5.5	21	1.3	30
Drosophila1	2	46.3	Poincaré	8.2	232	45.0	28
Drosophila1	3	38.7	Lorentz	10.5	248	37.1	29
Drosophila2	2	122.1	Mercator (full)	35.3	0	112.9	27
Drosophila2	3	112.2	Poincaré	11.8	1044	95.0	29
Human1	2	38.6	Lorentz	8.2	572	38.6	1
Human1	3	24.1	Mercator	14.9	26	17.8	28
Human2	2	43.2	Lorentz	9.9	602	40.1	7
Human2	3	26.4	Mercator	11.6	35	17.5	27
Human6	2	5.8	Mercator (full)	9.9	0	4.6	20
Human6	3	5.5	Mercator	9.2	15	2.1	30
Human7	2	6.1	Mercator (full)	8.5	0	5.1	30
Human7	3	5.2	Mercator	7.8	12	2.4	30
Human8	2	13.3	BFKL	4.0	2	10.6	30
Human8	3	10.1	Mercator	13.1	114	5.7	30
Macaque1	2	3.3	Poincaré	12.2	416	1.5	30
Macaque1	3	3.2	Poincaré	12.2	190	1.2	30
Macaque2	2	5.5	Lorentz	10.5	80	4.0	30
Macaque2	3	5.0	Lorentz	10.8	80	2.9	30
Macaque3	2	24.9	Poincaré	8.8	1392	23.4	30
Macaque3	3	21.3	Lorentz	9.7	253	17.6	30
Macaque4	2	1.3	Mercator (full)	14.0	0	0.2	30
Macaque4	3	1.2	Mercator	7.8	11	0.0	30
Mouse2	2	84.0	Lorentz	10.3	5172	80.7	29
Mouse2	3	71.3	Poincaré	12.2	5670	67.2	30
Mouse3	2	96.2	Lorentz	10.4	6068	92.4	29
Mouse3	3	83.8	Lorentz	12.4	6068	78.5	29
Rat1	2	4.9	Mercator (full)	23.5	0	7.1	0
Rat1	3	7.0	Lorentz	14.5	1647	8.7	0
Rat2	2	4.4	Mercator (full)	19.1	0	6.1	0
Rat2	3	7.3	Lorentz	14.5	1710	8.0	0
Rat3	2	5.4	Mercator (full)	20.8	0	6.5	0
Rat3	3	7.7	Poincaré	12.2	2407	7.8	4
ZebraFinch2	2	121.6	Mercator (full)	21.9	0	121.1	27
ZebraFinch2	3	115.9	Poincaré	6.2	3494	117.1	10

Table 13: Our embeddings vs. state-of-the-art. For each connectome and dimension, we list the best prior method and its result, the radius of the embedding, time elapsed in seconds, the best result of our method, and how many times (out of 30) our result was better. MeanRank measure.

connectome	dim	success	method	rad	time	ours	better
CElegans	2	0.903	Poincaré	7.2	267	0.931	27
CElegans	3	0.958	Poincaré	10.1	274	0.930	0
Cat1	2	1.000	Mercator (full)	9.9	0	1.000	0
Cat1	3	1.000	Lorentz	8.7	103	1.000	0
Cat2	2	1.000	Mercator (full)	12.6	0	0.986	0
Cat2	3	0.970	Poincaré	10.7	277	0.980	29
Cat3	2	1.000	Poincaré	10.3	96	1.000	0
Cat3	3	1.000	Poincaré	10.3	96	1.000	0
Drosophila1	2	0.783	Mercator (full)	24.6	0	0.847	29
Drosophila1	3	0.844	Poincaré	11.4	365	0.843	13
Drosophila2	2	0.761	Mercator (full)	35.3	0	0.560	0
Drosophila2	3	0.671	Poincaré	12.2	912	0.555	0
Human1	2	0.921	Lorentz	9.0	563	0.929	10
Human1	3	0.939	Lorentz	8.8	566	0.958	23
Human2	2	0.902	Lorentz	9.9	602	0.924	13
Human2	3	0.963	Lorentz	8.9	1344	0.961	14
Human6	2	0.996	BFKL	5.4	0	0.995	3
Human6	3	1.000	Lorentz	10.7	127	0.979	0
Human7	2	1.000	Lorentz	9.5	118	0.941	0
Human7	3	1.000	Lorentz	8.9	114	0.990	0
Human8	2	0.997	Mercator (full)	19.2	0	1.000	30
Human8	3	0.996	Poincaré	12.2	4856	0.997	30
Macaque1	2	0.997	Mercator (full)	17.8	0	0.990	6
Macaque1	3	0.980	Mercator	16.4	41	1.000	29
Macaque2	2	0.988	Mercator (full)	15.0	0	1.000	6
Macaque2	3	0.985	Poincaré	9.8	256	0.974	6
Macaque3	2	0.924	Mercator (full)	22.5	0	0.944	28
Macaque3	3	0.894	Poincaré	9.8	315	0.919	30
Macaque4	2	1.000	Mercator (fast)	16.1	0	1.000	0
Macaque4	3	1.000	Mercator	7.8	14	1.000	0
Mouse2	2	0.967	Mercator (full)	28.8	0	0.968	29
Mouse2	3	0.978	Lorentz	13.2	5176	0.959	0
Mouse3	2	0.962	Mercator (full)	34.5	0	0.967	30
Mouse3	3	0.971	Poincaré	12.2	8679	0.952	0
Rat1	2	0.998	Mercator (full)	26.1	0	0.960	0
Rat1	3	0.990	Lorentz	14.5	1664	0.899	0
Rat2	2	0.998	Mercator (full)	30.7	0	0.969	0
Rat2	3	0.993	Lorentz	14.5	1710	0.899	0
Rat3	2	0.998	Mercator (full)	20.8	0	0.958	0
Rat3	3	0.945	Lorentz	14.5	1836	0.906	0
ZebraFinch2	2	0.886	Mercator (full)	21.6	0	0.853	0
ZebraFinch2	3	0.889	Lorentz	6.3	1094	0.812	0

Table 14: Our embeddings vs. state-of-the-art. For each connectome and dimension, we list the best prior method and its result, the radius of the embedding, time elapsed in seconds, the best result of our method, and how many times (out of 30) our result was better. Greedy routing success measure.

connectome	dim	stretch	method	rad	time	ours	better
CElegans	2	1.310	Poincaré	7.2	278	1.254	30
CElegans	3	1.216	Poincaré	9.9	277	1.232	1
Cat1	2	1.046	Mercator (full)	9.6	0	1.046	18
Cat1	3	1.037	Lorentz	8.7	103	1.021	30
Cat2	2	1.053	Mercator (full)	12.6	0	1.058	7
Cat2	3	1.062	Poincaré	10.7	277	1.047	30
Cat3	2	1.042	Poincaré	9.7	291	1.039	23
Cat3	3	1.042	Lorentz	9.2	86	1.018	30
Drosophila1	2	1.402	Mercator (full)	24.6	0	1.340	28
Drosophila1	3	1.307	Lorentz	11.3	243	1.328	3
Drosophila2	2	1.202	Mercator (full)	35.3	0	1.964	0
Drosophila2	3	1.394	Poincaré	12.2	912	1.976	0
Human1	2	1.299	Lorentz	9.0	563	1.282	18
Human1	3	1.231	Lorentz	9.3	1554	1.176	27
Human2	2	1.298	Poincaré	11.3	3768	1.282	18
Human2	3	1.203	Poincaré	10.2	2977	1.177	25
Human6	2	1.059	BFKL	5.4	0	1.062	0
Human6	3	1.061	Lorentz	10.7	127	1.059	25
Human7	2	1.085	Mercator (full)	8.7	0	1.103	13
Human7	3	1.078	Lorentz	9.2	115	1.056	29
Human8	2	1.026	Lorentz	14.5	783	1.020	30
Human8	3	1.024	Poincaré	12.2	4856	1.017	30
Macaque1	2	1.025	Mercator (fast)	20.9	0	1.026	9
Macaque1	3	1.040	Mercator	16.4	41	1.019	30
Macaque2	2	1.069	Poincaré	12.2	88	1.056	5
Macaque2	3	1.065	Lorentz	10.8	80	1.068	16
Macaque3	2	1.180	Mercator (full)	22.9	0	1.169	18
Macaque3	3	1.194	Poincaré	10.2	1496	1.171	28
Macaque4	2	1.000	Mercator (fast)	16.1	0	1.000	0
Macaque4	3	1.000	Mercator	7.8	14	1.000	0
Mouse2	2	1.102	Mercator (full)	28.8	0	1.140	0
Mouse2	3	1.064	Lorentz	13.2	5176	1.120	0
Mouse3	2	1.108	Mercator (full)	29.8	0	1.156	0
Mouse3	3	1.077	Poincaré	12.2	9207	1.145	0
Rat1	2	1.003	Mercator (full)	21.4	0	1.048	0
Rat1	3	1.006	Lorentz	14.5	1664	1.120	0
Rat2	2	1.002	Mercator (full)	30.7	0	1.038	0
Rat2	3	1.004	Lorentz	14.5	1710	1.114	0
Rat3	2	1.005	Mercator (full)	20.8	0	1.059	0
Rat3	3	1.019	Mercator	17.4	471	1.105	0
ZebraFinch2	2	1.267	Mercator (full)	21.4	0	1.351	0
ZebraFinch2	3	1.323	Lorentz	6.1	1086	1.403	0

Table 15: Our embeddings vs. state-of-the-art. For each connectome and dimension, we list the best prior method and its result, the radius of the embedding, time elapsed in seconds, the best result of our method, and how many times (out of 30) our result was better. Greedy routing stretch measure.

the difference between these two cases is that the *big*-variant has a larger number of cells, this should not happen since any embedding in the standard variant is also an embedding in the *big*-variant. This is caused either by a failure to correctly guess the optimal values of the parameters or possibly because Simulated Annealing requires more iterations to find good embeddings at larger distances.

Our results stem from an extensive simulation scheme with numerous robustness checks. While our results regarding log-likelihood, MAP, and MeanRank were similar and robust to the changes in the Simulated Annealing setup, we noticed that optimizing log-likelihood may affect the quality measured by greedy success rate and stretch. We suspect that one explanation is that these two sets of quality measures capture different aspects (functions) of the networks. However, finding out the relationships among connectomes or embeddings characteristics and quality measures is beyond the scope of this paper and will be the subject of future work.

Acknowledgments

We wish to thank Piotr Pokarowski for his suggestions related to the presentation of the statistical analysis. We are also thankful to the anonymous referees for their suggestions. This work has been supported by the National Science Centre, Poland, grant UMO-2019/35/B/ST6/04456.

References

- [Ano24] Anonymous. Bridging ML and algorithms: comparison of hyperbolic embeddings, 2024. <https://openreview.net/forum?id=feZ7RpTLRy>.
- [AS20] Antoine Allard and M. Ángeles Serrano. Navigable maps of structural brain networks across species. *PLOS Computational Biology*, 16(2):1–20, 02 2020.
- [BFKK18] Thomas Bläsius, Tobias Friedrich, Maximilian Katzmann, and Anton Krohmer. Hyperbolic embeddings for near-optimal greedy routing. In *Algorithm Engineering and Experiments (ALENEX)*, pages 199–208, 2018.

- [BFKL16] Thomas Bläsius, Tobias Friedrich, Anton Krohmer, and Sören Laue. Efficient embedding of scale-free graphs in the hyperbolic plane. In *European Symposium on Algorithms (ESA)*, pages 16:1–16:18, 2016.
- [BPK10] Marián Boguñá, Fragkiskos Papadopoulos, and Dmitri Krioukov. Sustaining the internet with hyperbolic mapping. *Nature Communications*, 1(6):1–8, Sep 2010.
- [BS07] Mihail Bota and Larry W. Swanson. Online workbenches for neural network connections. *Journal of Comparative Neurology*, 500(5):807–814, 2007.
- [CFK⁺97] James W. Cannon, William J. Floyd, Richard Kenyon, Walter, and R. Parry. Hyperbolic geometry. In *In Flavors of geometry*, pages 59–115. University Press, 1997. Available online at <http://www.msri.org/communications/books/Book31/files/cannon.pdf>.
- [CK17] Dorota Celińska and Eryk Kopczyński. Programming languages in github: A visualization in hyperbolic plane. In *Proceedings of the Eleventh International Conference on Web and Social Media, ICWSM, Montréal, Québec, Canada, May 15-18, 2017.*, pages 727–728, Palo Alto, California, 2017. The AAAI Press.
- [CKK21] Dorota Celińska-Kopczyńska and Eryk Kopczyński. Discrete hyperbolic random graph model, 2021.
- [CKK24a] Dorota Celińska-Kopczyńska and Eryk Kopczyński, 2024. Supplementary material. https://figshare.com/articles/dataset/Modelling_brain_connectomes_networks_Solve_is_a_worthy_competitor_to_hyperbolic_geometry_/26352094.
- [CKK24b] Dorota Celińska-Kopczyńska and Eryk Kopczyński, 2024. Accompanying video. https://youtu.be/GQKaKF_yOL4.
- [CMST20] Rémi Coulon, Elisabetta A. Matsumoto, Henry Segerman, and Steve J. Trettel. Ray-marching thurston geometries, 2020.

- [CMST22] Remi Coulon, Sabetta Matsumoto, Henry Segerman, and Steve Trettel. 3-dimensional space, 2022. <https://3-dimensional.space/>.
- [Coh68] Jacob Cohen. Weighted kappa: Nominal scale agreement provision for scaled disagreement or partial credit. *Psychological Bulletin*, 70(4):213–220, 1968.
- [DSK⁺17] Sven Dorkenwald, Philipp J Schubert, Marius F Killinger, Gregor Urban, Shawn Mikula, Fabian Svara, and Joergen Kornfeld. Automated synaptic connectivity inference for volume electron microscopy. *Nat. Methods*, February 2017.
- [GPASB19] Guillermo García-Pérez, Antoine Allard, M Ángeles Serrano, and Marián Boguñá. Mercator: uncovering faithful hyperbolic embeddings of complex networks. *New Journal of Physics*, 21(12):123033, dec 2019.
- [GRKM⁺13] William Gray Roncal, Zachary H. Koterba, Disa Mhembere, Dean M. Kleissas, Joshua T. Vogelstein, Randal Burns, Anita R. Bowles, Dimitrios K. Donavos, Sephira Ryman, Rex E. Jung, Lei Wu, Vince Calhoun, and R. Jacob Vogelstein. Migraine: Mri graph reliability analysis and inference for connectomics. In *2013 IEEE Global Conference on Signal and Information Processing*, pages 313–316, 2013.
- [GSGR19] Albert Gu, Frederic Sala, Beliz Gunel, and Christopher Ré. Learning mixed-curvature representations in product spaces. In *Proc. ICLR*, pages 1–21. OpenReview.net, 2019.
- [HBT⁺13] Moritz Helmstaedter, Kevin L. Briggman, Srinivas C. Turaga, Viren Jain, H. Sebastian Seung, and Winfried Denk. Connectomic reconstruction of the inner plexiform layer in the mouse retina. *Nature*, 500:168–174, 2013.
- [HCG⁺08] Patric Hagmann, Leila Cammoun, Xavier Gigandet, Reto Meuli, Christopher Honey, Van Wedeen, and Olaf Sporns. Mapping the structural core of human cerebral cortex. *PLoS biology*, 6:e159, 08 2008.

- [HvdHS12] Logan Harriger, Martijn P. van den Heuvel, and Olaf Sporns. Rich club organization of macaque cerebral cortex and its role in network communication. *PLoS ONE*, 7, 2012.
- [JABS23] Robert Jankowski, Antoine Allard, Mari'an Bogun'a, and M. Ángeles Serrano. The d-mercator method for the multi-dimensional hyperbolic embedding of real networks. *Nature Communications*, 14, 2023.
- [KCK20] Eryk Kopczyński and Dorota Celińska-Kopczyńska. Real-time visualization in non-isotropic geometries, 2020.
- [KCK22] Eryk Kopczyński and Dorota Celińska-Kopczyńska. Real-time visualization in anisotropic geometries. *Experimental Mathematics*, 0(0):1–20, 2022.
- [KCK23] Eryk Kopczyński and Dorota Celińska-Kopczyńska. RogueViz: non-Euclidean geometry engine for visualizations, games, math art, and research, Oct 2023. <https://github.com/zenorogue/hyperrogue/>.
- [KH06] Marcus Kaiser and Claus C. Hilgetag. Nonoptimal component placement, but short processing paths, due to long-distance projections in neural systems. *PLoS Computational Biology*, 2, 2006.
- [KL16] Terry Koo and Mae Li. A guideline of selecting and reporting intraclass correlation coefficients for reliability research. *Journal of Chiropractic Medicine*, 15, 03 2016.
- [LK77] J. Richard Landis and Gary G. Koch. The measurement of observer agreement for categorical data. *Biometrics*, 33(1):159–174, 1977.
- [LRP95] John Lamping, Ramana Rao, and Peter Pirolli. A focus+context technique based on hyperbolic geometry for visualizing large hierarchies. In *Proceedings of the SIGCHI Conference on Human Factors in Computing Systems, CHI '95*, pages 401–408, New York, NY, USA, 1995. ACM Press/Addison-Wesley Publishing Co.

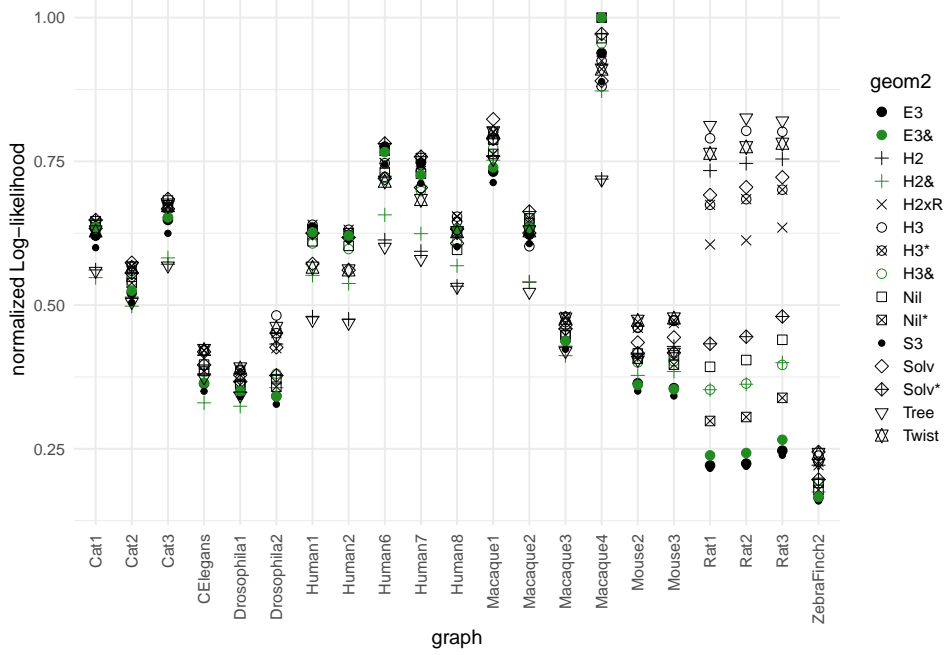
- [MD04] Eric Maskin and Partha Dasgupta. The fairest vote of all. *Scientific American*, 290(3):64–69, 2004.
- [MERL⁺13] Nikola Markov, Mária Ercsey-Ravasz, Camille Lamy, Ana Rita, Ana Ribeiro Gomes, Loïc Magrou, Pierre Misery, Pascale Giroud, Pascal Barone, Colette Dehay, Zoltan Toroczkai, Kenneth Knoblauch, David Essen, and Henry Kennedy. The role of long-range connections on the specificity of the macaque interareal cortical network. *Proceedings of the National Academy of Sciences*, 110, 03 2013.
- [Mun98] Tamara Munzner. Exploring large graphs in 3d hyperbolic space. *IEEE Computer Graphics and Applications*, 18(4):18–23, 1998.
- [NK17] Maximilian Nickel and Douwe Kiela. Poincaré embeddings for learning hierarchical representations. In I. Guyon, U. V. Luxburg, S. Bengio, H. Wallach, R. Fergus, S. Vishwanathan, and R. Garnett, editors, *Advances in Neural Information Processing Systems 30*, pages 6341–6350. Curran Associates, Inc., 2017.
- [NK18] Maximilian Nickel and Douwe Kiela. Learning continuous hierarchies in the lorentz model of hyperbolic geometry. In Jennifer G. Dy and Andreas Krause, editors, *Proceedings of the 35th International Conference on Machine Learning, ICML 2018, Stockholmsmässan, Stockholm, Sweden, July 10-15, 2018*, volume 80 of *Proceedings of Machine Learning Research*, pages 3776–3785. PMLR, 2018.
- [PKS⁺12] Fragkiskos Papadopoulos, Maksim Kitsak, M. Angeles Serrano, Marian Boguñá, and Dmitri Krioukov. Popularity versus Similarity in Growing Networks. *Nature*, 489:537–540, Sep 2012.
- [Rog22] Zeno Rogue. Nil geometry explained!, 2022. <https://www.youtube.com/watch?v=FNX1rZotjJI>.
- [Rog23] Zeno Rogue. Non-euclidean third dimension in games, 2023. https://www.youtube.com/watch?v=Rhju_PazzZE (includes an explanation of Solv).

- [SBH⁺99] Jack W. Scannell, Gully A. Burns, Claus C. Hilgetag, Molly A. O’Neil, and Malcolm P. Young. The connectional organization of the cortico-thalamic system of the cat. *Cerebral cortex*, 9 3:277–99, 1999.
- [SBY95] JW Scannell, Colin Blakemore, and MP Young. Analysis of connectivity in the cat cerebral cortex. In *Journal of Neuroscience*, 1995.
- [Sch20] Richard Evan Schwartz. personal communication, 2020. *I once heard a talk (at MSRI, 1992) by a biologist talking about brain architecture. Thurston was in the audience and he claimed that "parts of our brain are modeled on Sol". Or maybe he said that they might be modelled on Sol. Nobody knew what he was talking about, but it was intriguing. It was the first time I had heard of Sol being useful for anything (besides uniformizing Anosov torus bundles.) (My memory about this is perhaps a bit hazy.)*
- [SDSGR18] Frederic Sala, Chris De Sa, Albert Gu, and Christopher Re. Representation tradeoffs for hyperbolic embeddings. In *Proc. ICML*, pages 4460–4469, Stockholmsmässan, Stockholm Sweden, 2018. PMLR.
- [SF79] Patrick Shrout and Joseph Fleiss. Intraclass correlations: Uses in assessing rater reliability. *Psychological bulletin*, 86:420–8, 03 1979.
- [SNM⁺22] Kazunori Shinomiya, Aljoscha Nern, Ian A. Meinertzhagen, Stephen M. Plaza, and Michael B. Reiser. Neuronal circuits integrating visual motion information in drosophila melanogaster. *Current Biology*, 32(16):3529–3544.e2, 2022.
- [Thu82] William P. Thurston. Three dimensional manifolds, Kleinian groups and hyperbolic geometry. *Bulletin (New Series) of the American Mathematical Society*, 6(3):357–381, may 1982.
- [VCP⁺11] Lav R. Varshney, Beth L. Chen, Eric Paniagua, David H. Hall, and Dmitri B. Chklovskii. Structural properties of the

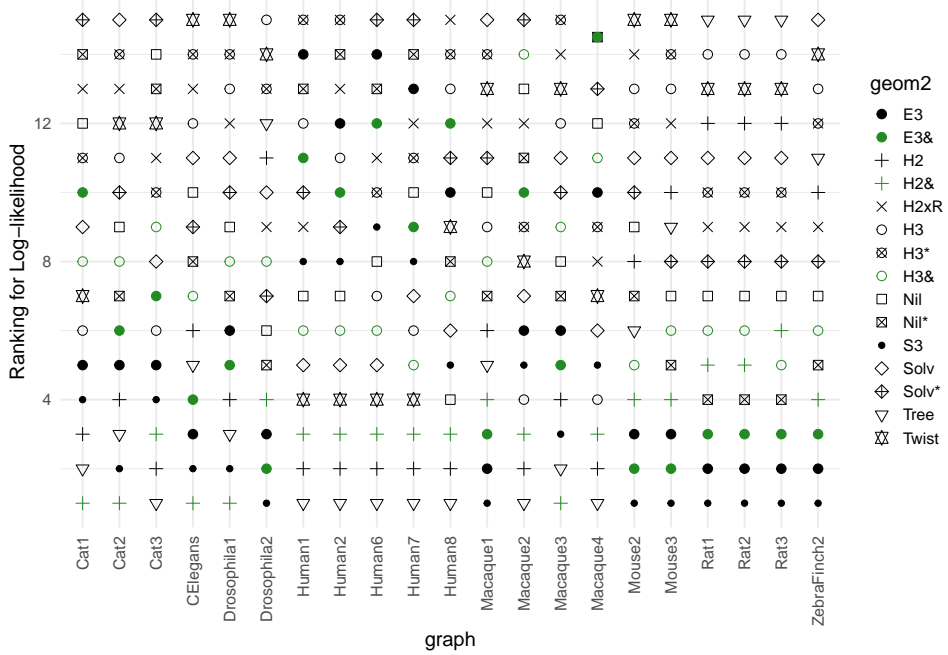
caenorhabditis elegans neuronal network. *PLOS Computational Biology*, 7(2):1–21, 02 2011.

[WHKL22] Wonseok Whi, Seunggyun Ha, Hyejin Kang, and Dong Soo Lee. Hyperbolic disc embedding of functional human brain connectomes using resting-state fMRI. *Network Neuroscience*, 6(3):745–764, 07 2022.

[You93] Malcolm P. Young. The organization of neural systems in the primate cerebral cortex. *Proceedings: Biological Sciences*, 252(1333):13–18, 1993.

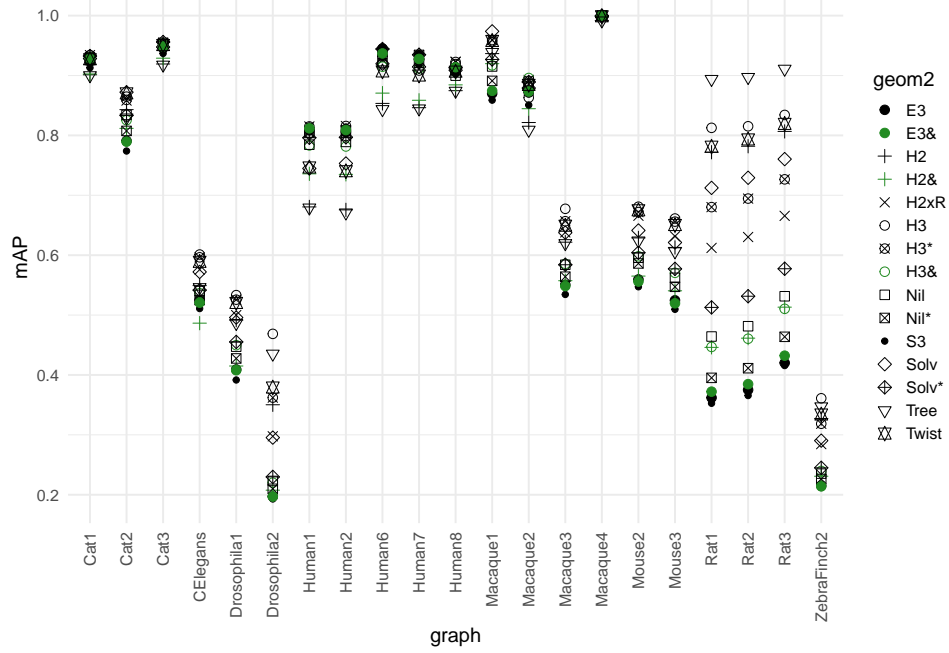


(a) Normalized log-likelihood

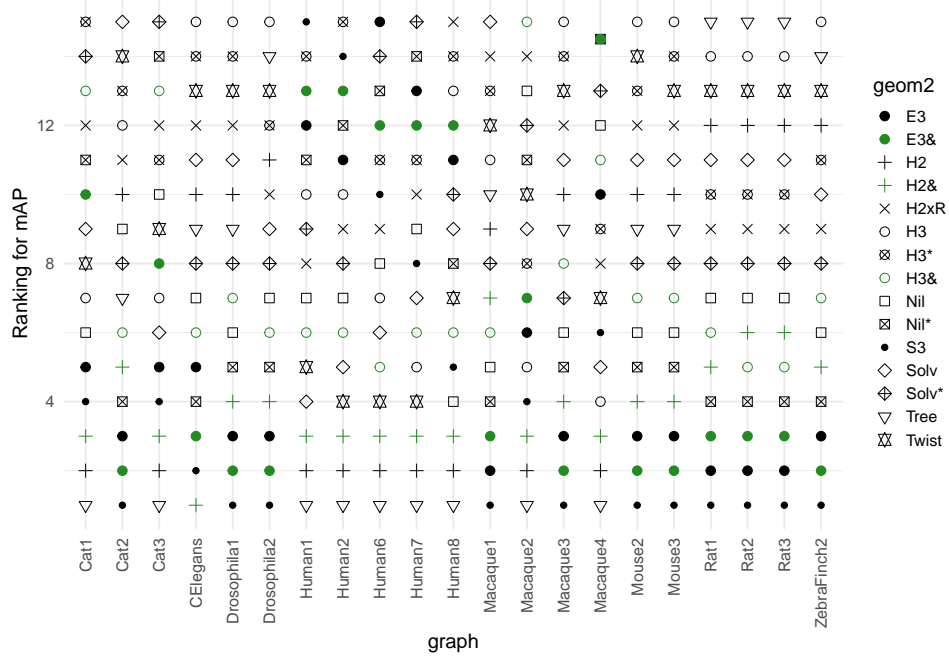


(b) Normalized log-likelihood – ranks

Figure 3: Our best embeddings – log-likelihood. Top = best embedding obtained, bottom = worst embedding obtained, * = fine grid.

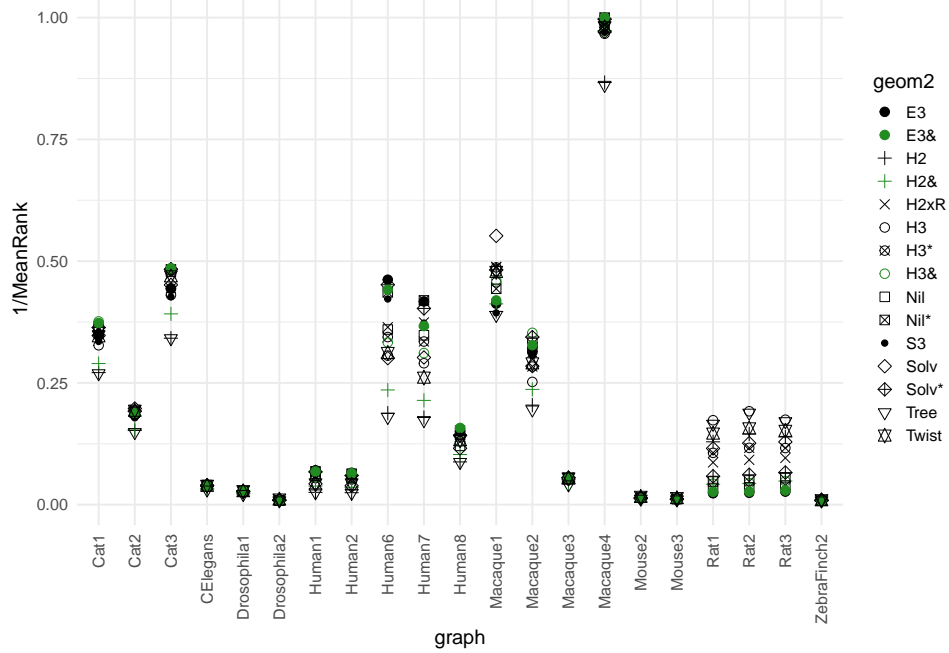


(a) mAP

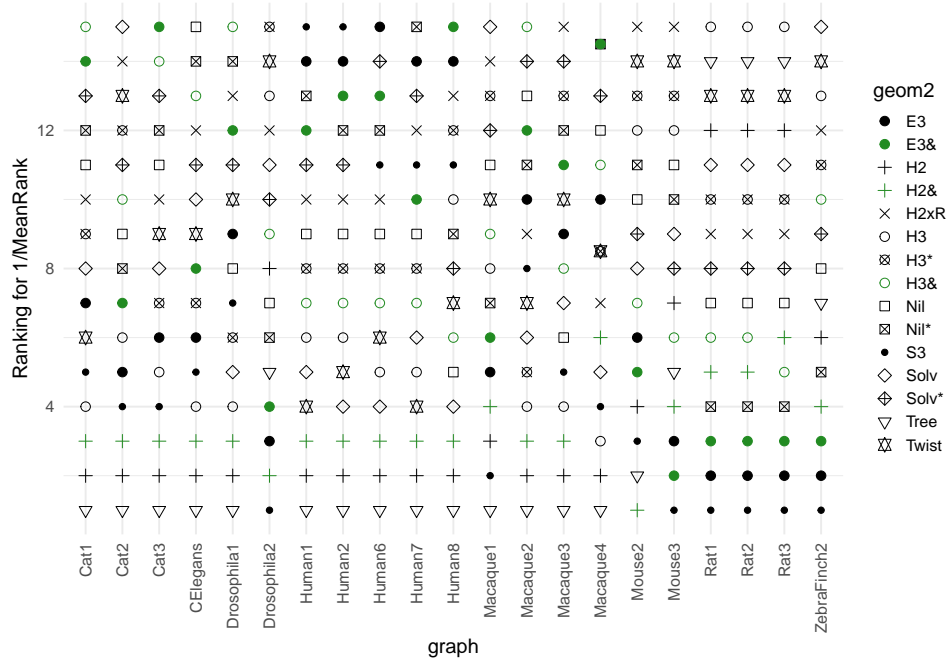


(b) mAP – ranks

Figure 4: Our best embeddings – mAP. Top = best embedding obtained, bottom = worst embedding obtained, $37_{\#}$ = fine grid.

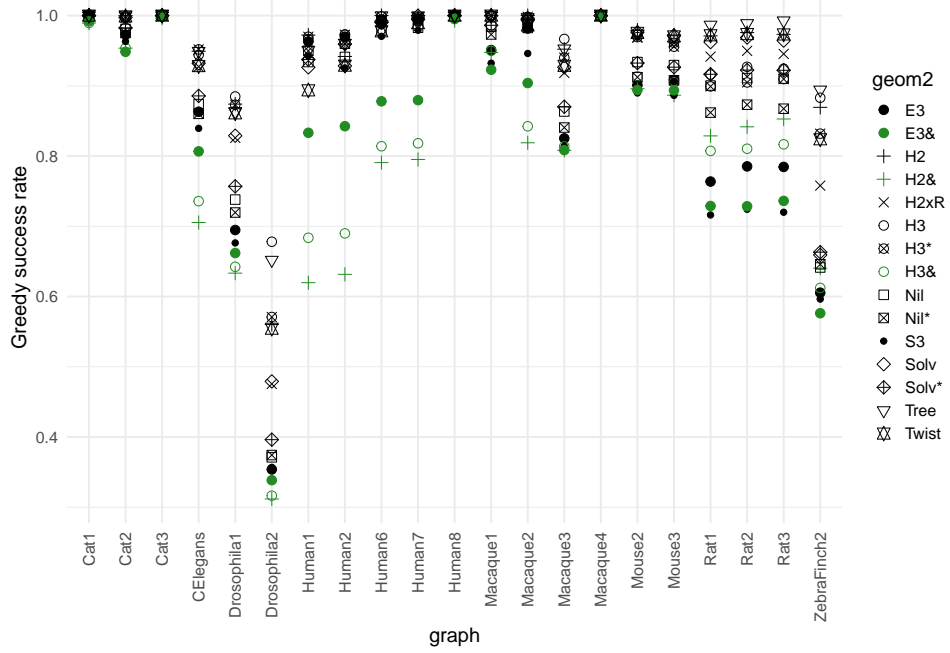


(a) 1/MeanRank

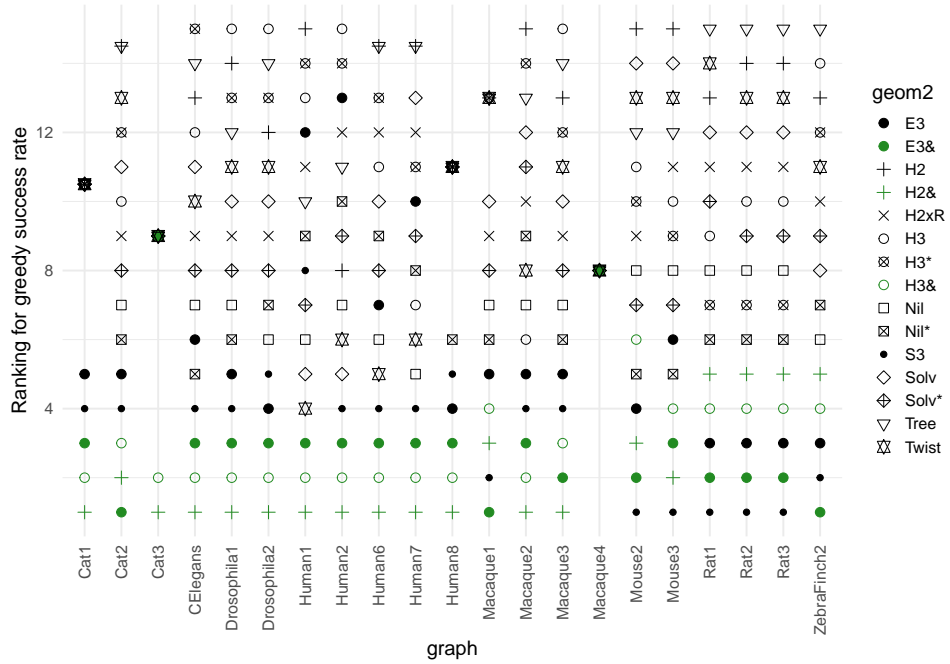


(b) 1/MeanRank – ranks

Figure 5: Our best embeddings – MeanRank. Top = best embedding obtained, bottom = worst embedding obtained, * = fine grid.

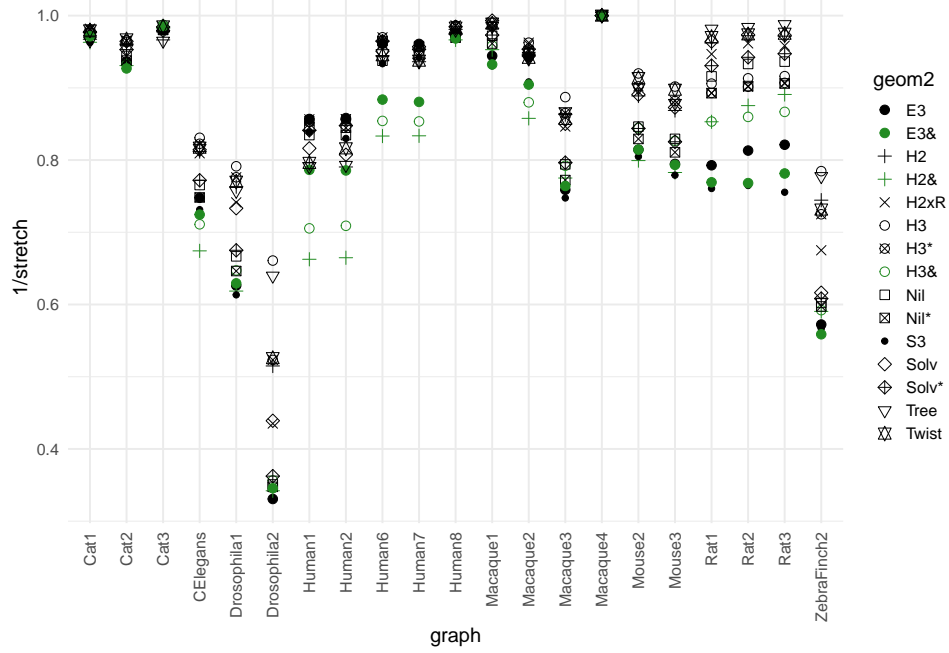


(a) Greedy success rate

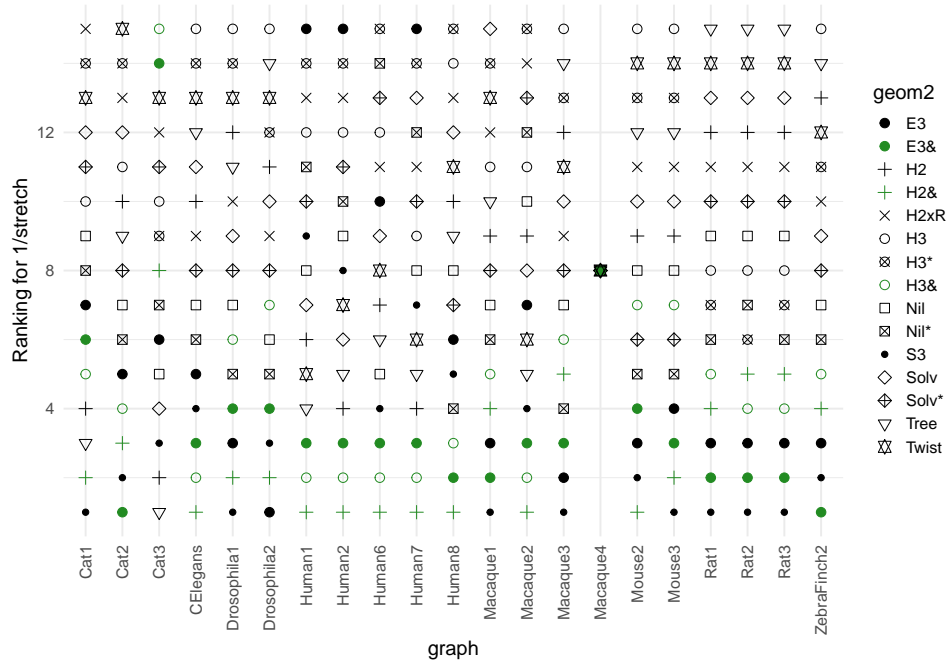


(b) Greedy success rate – ranks

Figure 6: Our best embeddings – greedy success rate. Top = best embedding obtained, bottom = worst embedding obtained, * = fine grid.



(a) 1/stretch



(b) 1/stretch – ranks

Figure 7: Our best embeddings – stretch. Top = best embedding obtained, bottom = worst embedding obtained, 40^k = fine grid.

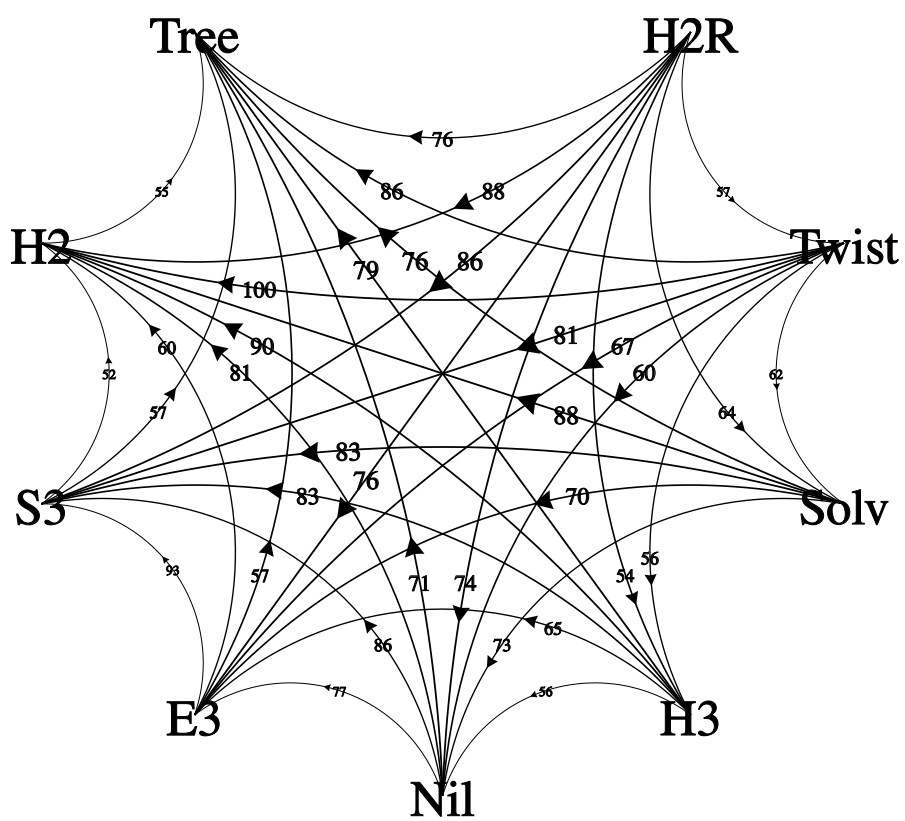


Figure 8: Normalized log-likelihood

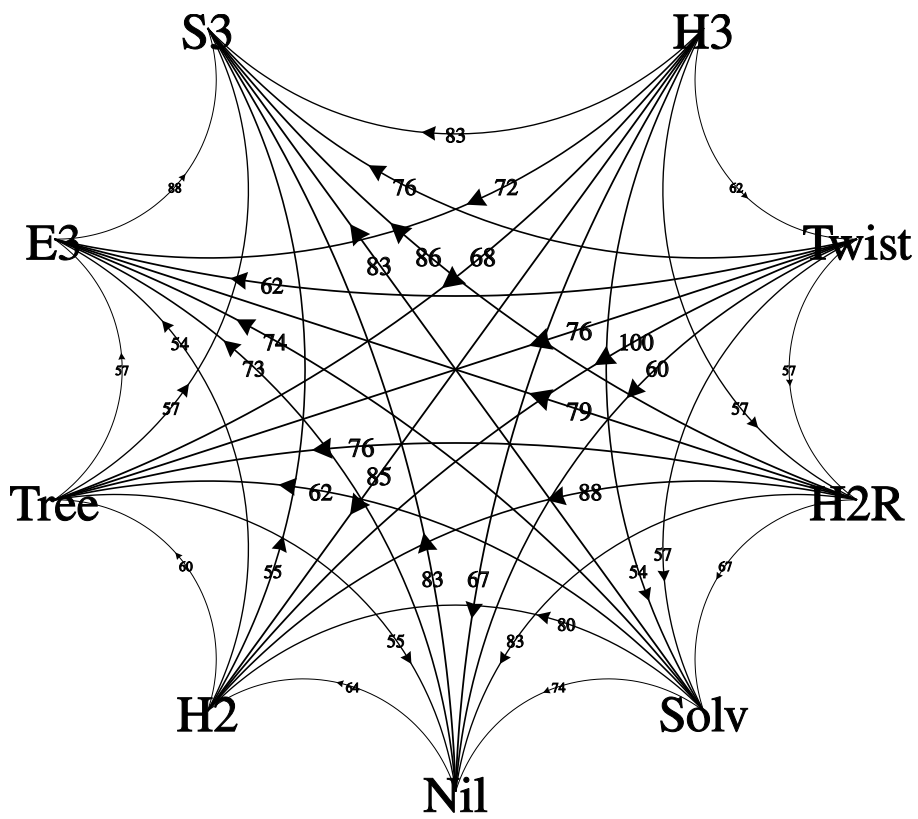


Figure 9: MAP

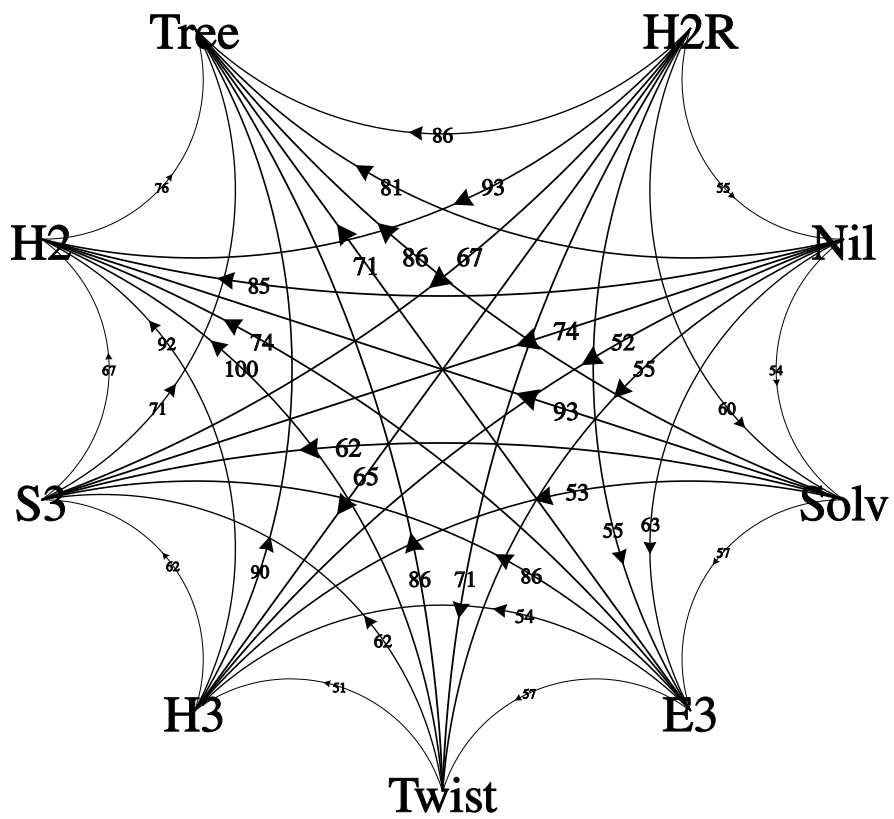


Figure 10: IMR

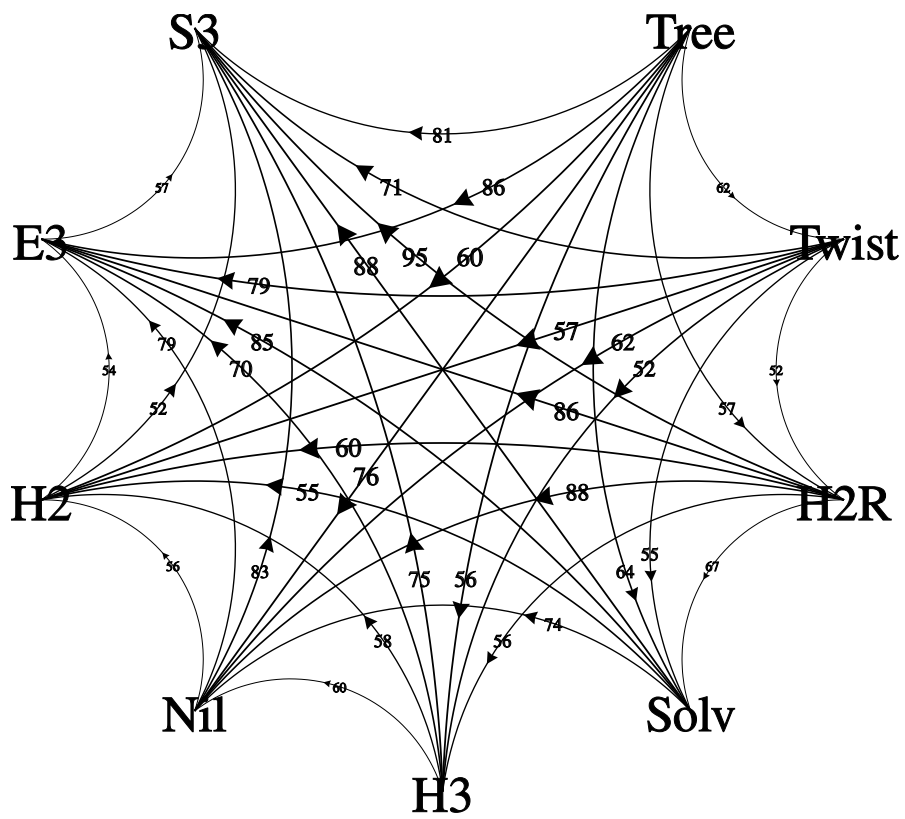


Figure 11: SC

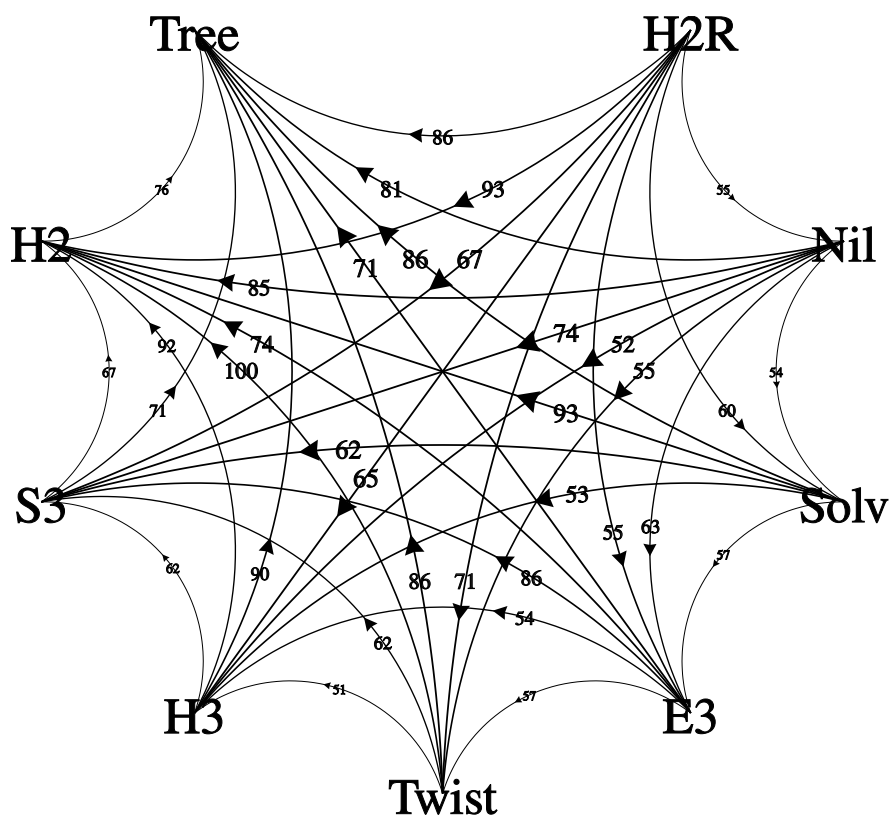


Figure 12: ISTR

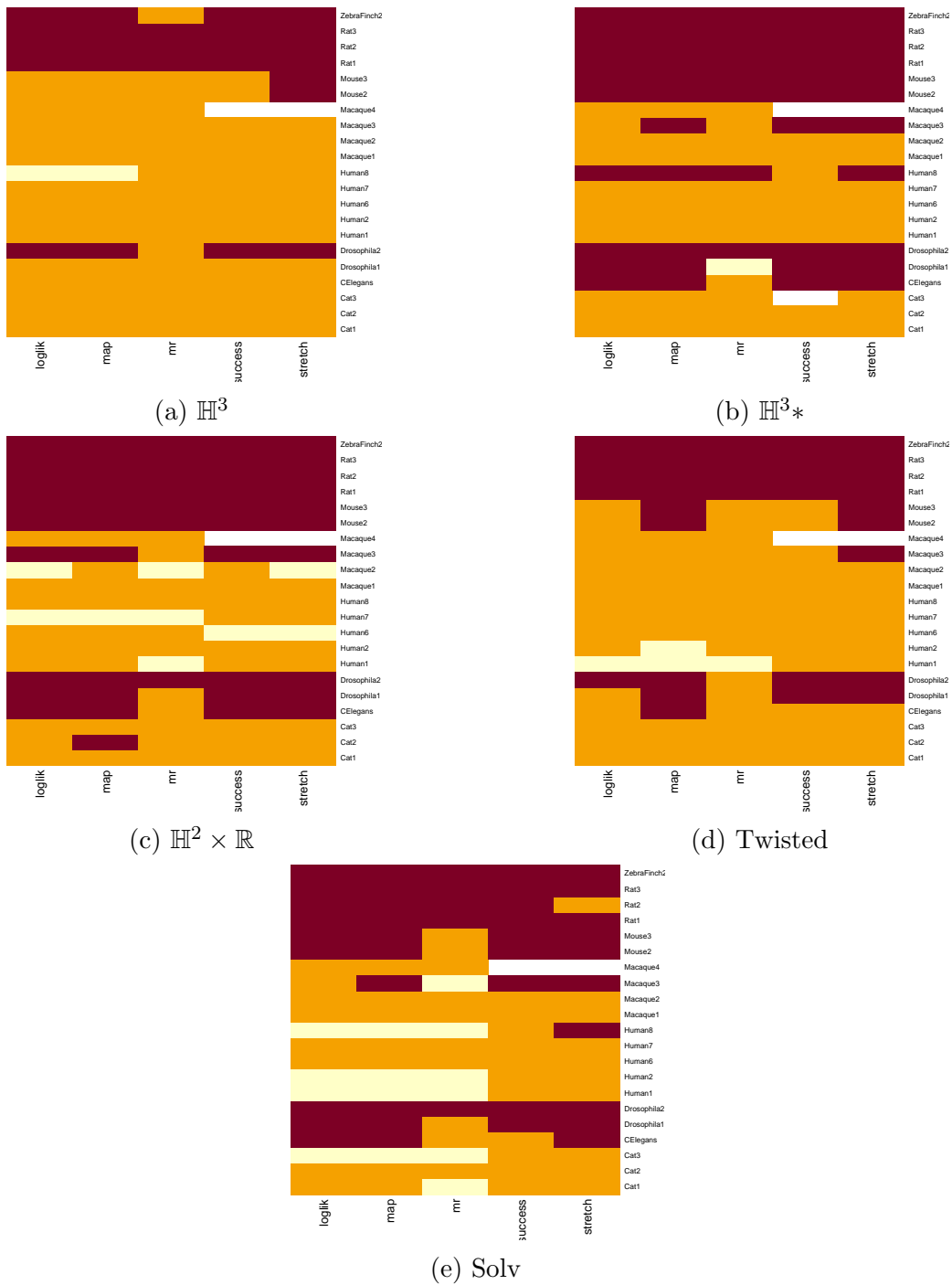


Figure 13: Comparison of the goodness of fit between regular and *big* versions of manifolds. Red suggests that the *big* version yields better results and the difference is significant; orange suggests lack of significant difference, and yellow suggests significantly worse results for *big* version.

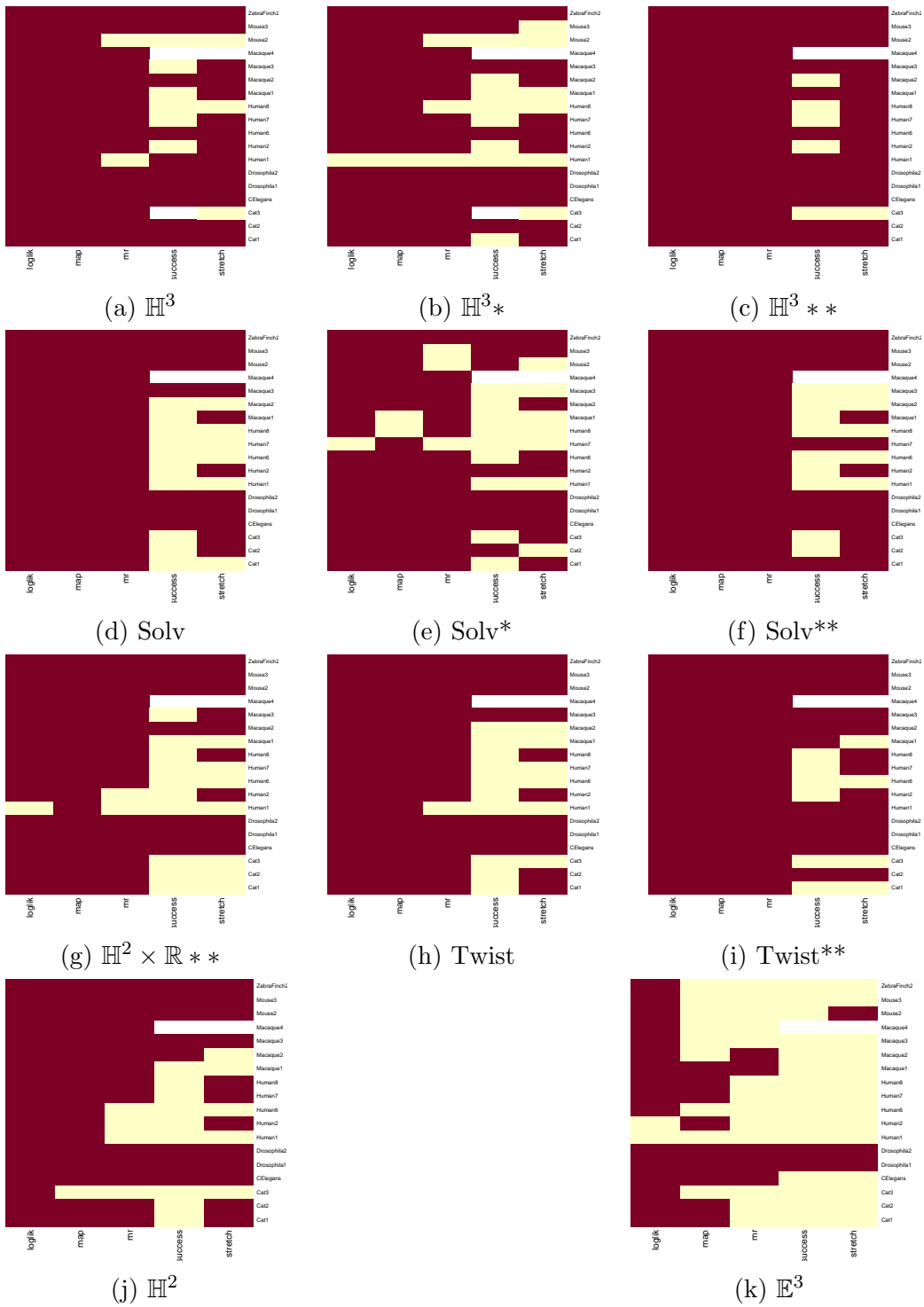
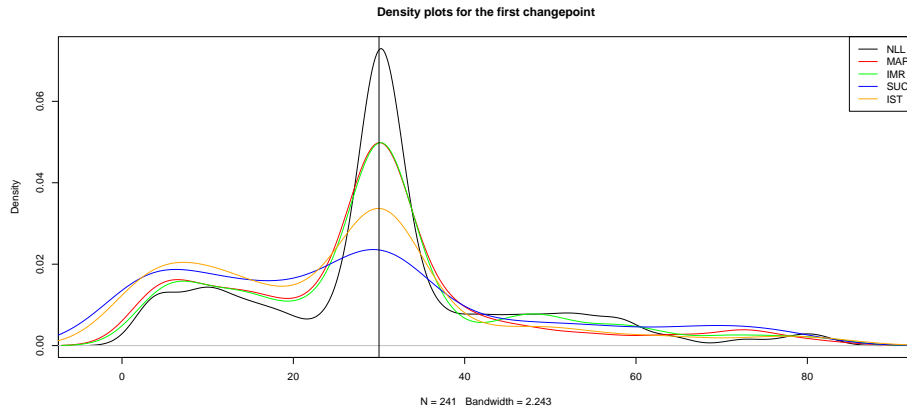
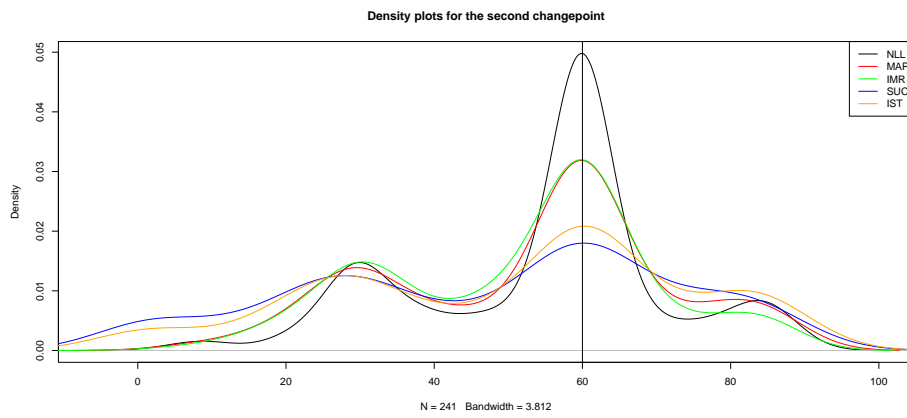


Figure 14: Comparison of the goodness of fit between results of Simulated Annealing with 10.000 vs. 100.000 steps per iteration. Red suggests that the longer version yields better results and the difference is significant; orange suggests lack of significant difference, and yellow suggests significantly worse results for longer version.



(a) First changepoint



(b) Second changepoint

Figure 15: Density plots for changepoints in time series of measures (indicators for level shifts)

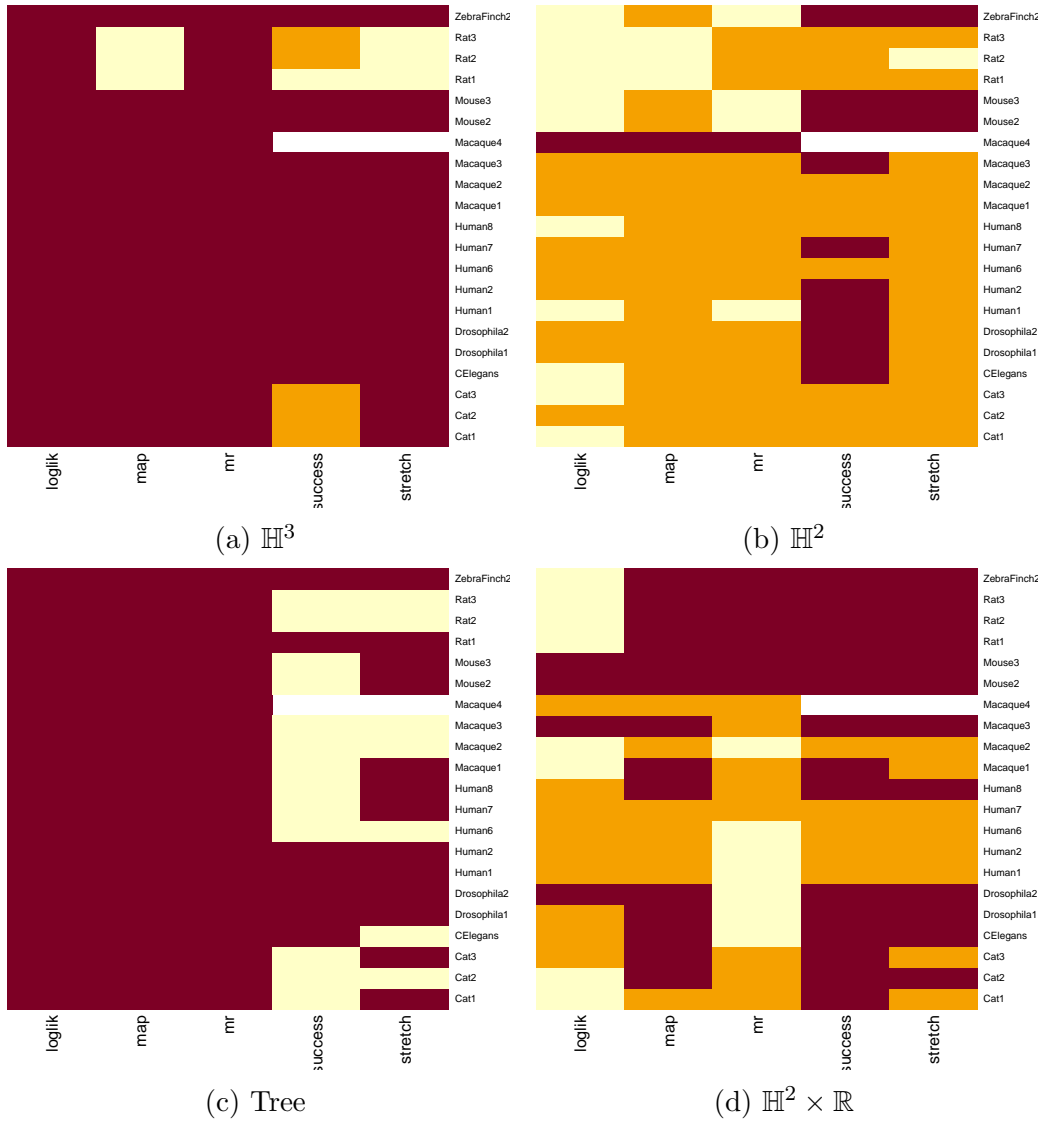


Figure 16: Comparison of the goodness of fit between pairs of tessellations. Red suggests that the continuous (non-angular) version yields better results and the difference is significant; orange suggests lack of significant difference, and yellow suggests significantly worse results for continuous (non-angular) version, respectively.